UNCLASSIFIED

AD NUMBER
ADB003672
LIMITATION CHANGES
TO: **Approved for public release; distribution is unlimited.**
FROM: **Distribution authorized to U.S. Gov't. agencies only; Test and Evaluation; APR 1975. Other requests shall be referred to Air Force Armament Lab., Eglin AFB, FL.**
AUTHORITY
AFATL ltr 26 May 1977

THIS PAGE IS UNCLASSIFIED

AEDC-TR-75-32
AFATL-TR-75-45

A WIND TUNNEL EVALUATION OF AN FMU-110B FUZE MOUNTED ON AN SUU-30 DISPENSER AT MACH NUMBERS FROM 0.20 TO 1.40

J. A. Collins
ARO, Inc.

PROPULSION WIND TUNNEL FACILITY
ARNOLD ENGINEERING DEVELOPMENT CENTER
AIR FORCE SYSTEMS COMMAND
ARNOLD AIR FORCE STATION, TENNESSEE 37389

April 1975

Final Report for Period November 25–26, 1974

Distribution limited to U.S. Government agencies only; this report contains information on test and evaluation of military hardware; April 1975; other requests for this document must be referred to Air Force Armament Laboratory (DLJF), Eglin AFB, Florida 32542.

Prepared for

AIR FORCE ARMAMENT LABORATORY (DLJF)
EGLIN AFB, FLORIDA 32542

NOTICES

APPROVAL STATEMENT

This technical report has been reviewed and is approved for publication.

FOR THE COMMANDER

Lamar R. Kissling

LAMAR R. KISSLING
Lt Colonel, USAF
Chief Air Force Test Director, PWT
Directorate of Test

Frank J. Passarello

FRANK J. PASSARELLO
Colonel, USAF
Director of Test

REPORT DOCUMENTATION PAGE

READ INSTRUCTIONS BEFORE COMPLETING FORM

1. REPORT NUMBER
AEDC-TR-75-32
AFATL-TR-75-45

2. GOVT ACCESSION NO.

3. RECIPIENT'S CATALOG NUMBER

4. TITLE (and Subtitle)
A WIND TUNNEL EVALUATION OF AN FMU-110B FUZE MOUNTED ON AN SUU-30 DISPENSER AT MACH NUMBERS FROM 0.20 TO 1.40

5. TYPE OF REPORT & PERIOD COVERED
Final Report- November 25-26, 1974

6. PERFORMING ORG. REPORT NUMBER

7. AUTHOR(s)
J. A. Collins, ARO, Inc.

8. CONTRACT OR GRANT NUMBER(s)

9. PERFORMING ORGANIZATION NAME AND ADDRESS
Arnold Engineering Development Center (XO)
Arnold Air Force Station, Tennessee 37389

10. PROGRAM ELEMENT, PROJECT, TASK AREA & WORK UNIT NUMBERS
Program Element 64602F
Project 4432-03

11. CONTROLLING OFFICE NAME AND ADDRESS
Air Force Armament Laboratory (DLJF)
Eglin AFB, Florida 32542

12. REPORT DATE
April 1975

13. NUMBER OF PAGES
64

14. MONITORING AGENCY NAME & ADDRESS (if different from Controlling Office)

15. SECURITY CLASS. (of this report)
UNCLASSIFIED

15a. DECLASSIFICATION/DOWNGRADING SCHEDULE
N/A

16. DISTRIBUTION STATEMENT (of this Report)
Distribution limited to U.S. Government agencies only; this report contains information on test and evaluation of military hardware; April 1975; other requests for this document must be referred to Air Force Armament Laboratory (DLJF), Eglin AFB, Florida 32542.

17. DISTRIBUTION STATEMENT (of the abstract entered in Block 20, if different from Report)

18. SUPPLEMENTARY NOTES
Available in DDC

19. KEY WORDS (Continue on reverse side if necessary and identify by block number)

wind tunnel tests	radomes
FMU-110B fuze	angle of attack
SUU-30 bomb dispenser	roll
Mach numbers	angles

20. ABSTRACT (Continue on reverse side if necessary and identify by block number)

Results are presented of a wind tunnel evaluation of an FMU-110B fuze which was mounted on the radome protruding from the nose of an SUU-30 bomb dispenser (full scale). The test was conducted at Mach numbers from 0.20 to 1.40, at angles of attack from -10 to 10 deg, and at roll angles from 0 to 180 deg.

PREFACE

The work reported herein was conducted by the Arnold Engineering Development Center (AEDC), Air Force Systems Command (AFSC), at the request of the Air Force Armament Laboratory for the Government Electronics Division of Motorola, Incorporated, under Program Element 64602F, Project No. 4432-03. The project monitor was Mr. T. Britton, AFATL/DLJF. The results were obtained by ARO, Inc. (a subsidiary of Sverdrup & Parcel and Associates, Inc.), contract operator of AEDC, AFSC, Arnold Air Force Station, Tennessee. The work was done under ARO Project No. P41T-76A. Data reduction was completed on December 13, 1974, and the manuscript (ARO Control No. ARO-PWT-TR-75-9) was submitted for publication on January 29, 1975.

CONTENTS

ILLUSTRATIONS

Figure		Page

1.0 INTRODUCTION

The objective of the test was to evaluate the differential pressure produced by the venturi which was an integral part of the FMU-110B fuze. Pressure data were obtained from the internal flow through the venturi and on the external surface of the FMU-110B-modified SUU-30 flight configuration at Mach numbers from 0.2 to 1.4. Model angles of attack were varied from -10 to 10 deg, and roll angles were varied from 0 to 180 deg.

2.0 APPARATUS

2.1 TEST FACILITY

Tunnel 16T is a closed-circuit, continuous flow tunnel that can be operated at Mach numbers from 0.20 to 1.60. The test section is 16 by 16 ft in cross section and is 40 ft long. The tunnel can be operated within a stagnation pressure range from 120 to 4000 psfa, depending on the Mach number. Perforated test section walls allow continuous operation through the Mach number range with a minimum of wall interference. Additional information on the tunnel, its capabilities, and supporting equipment may be found in the Test Facilities Handbook.[1]

2.2 MODEL SUPPORT SYSTEM

The model was sting mounted in the test section on the standard sting support system which is capable of pitching from -11 to 11 deg and rolling through ±180 deg. The pitch center of the model support system was such that the model remained essentially on the tunnel centerline throughout its pitch range. The location of the model in the test section is shown in Fig. 1.

2.3 TEST ARTICLE

The test article was a full-scale, flight hardware FMU-110B fuze which was mounted on the radome protruding from the nose of an SUU-30 bomb dispenser which was modified to two body diameters in length. A photograph of the model in the test section is shown in Fig. 2, and a dimensional sketch of the model is presented in Fig. 3.

The hardware contained two pressure orifices near the throat of the fuze venturi which connected to a pressure switch in the flight vehicle as shown in Fig. 3b. These orifices were utilized along with an additional pressure orifice into the interior of the

---

[1] Test Facilities Handbook (Tenth Edition). "Propulsion Wind Tunnel Facility, Vol. 4." Arnold Engineering Development Center, May 1974.

venturi and several orifices on the exterior of the wedge-shaped structure containing the fuze venturi. The geometry of these orifices is shown in Fig. 4 along with a tabulation listing the external pressure orifices on the radome face. These external pressures consisted of orifices located in four rows placed at radial orientations of 0, 90, 180, and -90 deg. The four rows of pressure orifices on the radome were extended along the SUU-30 neck and body for a total model length distance of 0.478 in. as shown in Fig. 5. Seam construction of the SUU-30 dispenser made it necessary to offset two rows of orifices on the bomb body by 5 deg to the -85- and 95-deg radial.

2.4 INSTRUMENTATION

Steady-state pressures were measured utilizing the facility's pressure system which connected each pressure to an individual transducer. All pressures were monitored by a real-time static pressure indicator (profile monitor).

Model gravimetric angle of attack was measured by means of a model-mounted, absolute angle-of-attack sensor. All instrumentation were scanned into an on-line computer system which reduced the raw data to engineering units, computed pertinent parameters, and tabulated and plotted data on a Cathode-Ray Tube (CRT).

3.0 PROCEDURES

3.1 TEST PROCEDURE

After the tunnel's free-stream conditions were established, data were obtained at various model pitch and roll angles. In order to account for pressure lag, 20 seconds were allowed between moving the model and acquisition of the test data.

3.2 PRECISION OF MEASUREMENTS

Uncertainties (bands which include 95 percent of the calibration data) of the basic tunnel parameters, free-stream total pressure (P_{t_∞}), total temperature (T_{t_∞}), and free-stream Mach number (M_∞) were estimated from repeat calibrations of the instrumentation and from the repeatability and uniformity of the test section flow during tunnel calibrations. These estimates were then used to determine uncertainties of other free-stream properties, free-stream static pressure (P_∞), and free-stream dynamic pressure (q_∞) using the Taylor series method of error propagation:

M_∞	ΔM_∞	ΔP_{t_∞},psf	ΔP_∞,psf	Δq_∞,psf	ΔCP
0.20	±0.0030	±1.5999	±2.02151	±0.0095	±0.0496
0.40	±0.0012	±1.6000	±1.7112	±0.8753	±0.0127
0.60	±0.0016	±1.6500	±2.47697	±1.6359	±0.0096
0.95	±0.0048	±1.5324	±4.71097	±2.5847	±0.0112
1.40	±0.0120	±1.5013	±7.99341	±0.6694	±0.0125

Calculation of the model angles of attack and sideslip are considered precise within ±0.1 deg.

4.0 RESULTS AND DISCUSSION

The primary purpose of this test was to evaluate the aerodynamic performance of the venturi which was an integral part of the FMU-110B fuze mounted on the nose of an ~~SUU~~-30 bomb dispenser. A secondary objective of this test was to map the external flow environment of the fuze-radome-bomb configuration. Figures 4 and 5 contain tabulations which correlate pressure orifice numbers to their respective locations. A representative segment of the data is presented herein.

4.1 FUZE PERFORMANCE

The pressure differential in inches of water was measured at the two venturi orifices shown in Fig. 3, and its variation with angle of attack and sideslip angle are presented in Figs. 6 through 9. The pressure differential varied a maximum of 4 in. of water for angles of attack of -6 to 6 deg as shown in Fig. 6. At low subsonic Mach numbers ($M_\infty \leqslant 0.40$) the pressure differential remained essentially constant for -10 $\leqslant$ angle of attack $\leqslant$ 10 deg except for a distinct peak value at -8-deg angle of attack. For Mach numbers of 0.95 to 1.40 (venturi choking conditions), the venturi differential pressure showed some small variations at all angles of attack. The influence of sideslip angle on the differential pressure is shown in Fig. 7. The variation in venturi differential pressure was less than 2 in. of water for sideslip angles from -5 to 5 deg. After choking occurred, the pressure differential was invariable for all of the selected beta angles. A small increment in differential pressure was due to pressure altitude changes as is evident in Figs. 8 and 9 for alpha and beta sweeps, respectively.

4.2 EXTERNAL PRESSURE PROFILES

4.2.1 Effects of Angle of Attack

The pressure profiles on the radome face utilized the orifices shown in Fig. 4. The variation in angle of attack had little influence on the radome-face pressure profiles throughout the Mach number range as shown in Fig. 10.

The external pressure profiles on the radome-bomb dispenser for the top (100) and bottom (300) rows are shown in Figs. 11 through 13, respectively. The data in Fig. 11 show the effect of -10-deg angle of attack on the pressure along the top and bottom rows for Mach numbers of 0.20 through 1.40. A typical trend shown was the increase in static pressure along the radome and bomb neck. Flow acceleration around the blunt SUU-30 nose caused the static pressure to decrease along the bomb until the flow along the bomb stabilized. At supersonic speeds, flow disturbances in the bomb neck region resulted in breaks in the pressure pattern for the pressure orifices on the top row with a uniform subsonic profile being maintained.

Figure 12 shows the symmetrical similarity of the pressure profiles along the top and bottom rows on this near symmetrical model at zero angle of attack. Flow separation over the aft end of the radome created a high-pressure area on the forward portion of the bomb. Again, flow acceleration around the blunt nose of the bomb created lower static pressures.

The external flow characteristics of the radome-bomb body at 10-deg angle of attack are presented in Fig. 13. A reverse in the pressure profiles from those in Fig. 11 is shown in Fig. 13 with the bottom row having the higher static pressures.

Figures 14 through 16 present typical external pressure distribution patterns on the radome, bomb sides along the number 200 and 400 pressure rows (radome, bomb neck θ = -90, 90 deg, bomb side θ = -85, 95 deg) with the model pitched to -10, 0, and 10 deg, respectively. The trend of the pressure variations along the sides of the radome-bomb neck and the blunt bomb nose was similar to that along the top and bottom rows at $\alpha = 0$.

4.2.2 Effects of Sideslip Angle

Negligible influence from various sideslip angles on the pressure profiles on the radome face for representative Mach numbers is shown in Fig. 17. Data in Figs. 18 through 23 present the static pressure variations along the radome side-bomb body configuration while varying beta angle at Mach numbers 0.20 through 1.40. Figures 18 through 20 show data for the top and bottom rows during pure beta sweeps, rows 200 and 400 are located at θ = -90 and 90 deg on the radome and bomb neck, with θ = -85 and 95 deg locations on the bomb body. The trend noted in the pure alpha sweeps is again present for these beta angles. Good symmetrical similarity is shown at beta angles of -10, -0.5, and 9.5 deg for the two side rows in Figs. 21 through 23.

5.0 CONCLUDING REMARKS

Pressure data taken on the internal venturi flow and the external surface pressure pattern on the radome-bomb body produced the following results:

1. The pressure differential across the venturi, which was an integral part of the fuze, showed little change at angles of attack from -6 to 6 deg and sideslip angles from -5 to 5 deg.

2. Static pressure profiles measured on the top and bottom of the symmetrical radome-SUU-30 bomb configuration for both alpha and beta sweeps showed an increased value along the radome-bomb neck. Flow acceleration around the semi-blunted bomb nose produced a decreasing static pressure until stabilization of the flow along the bomb occurred.

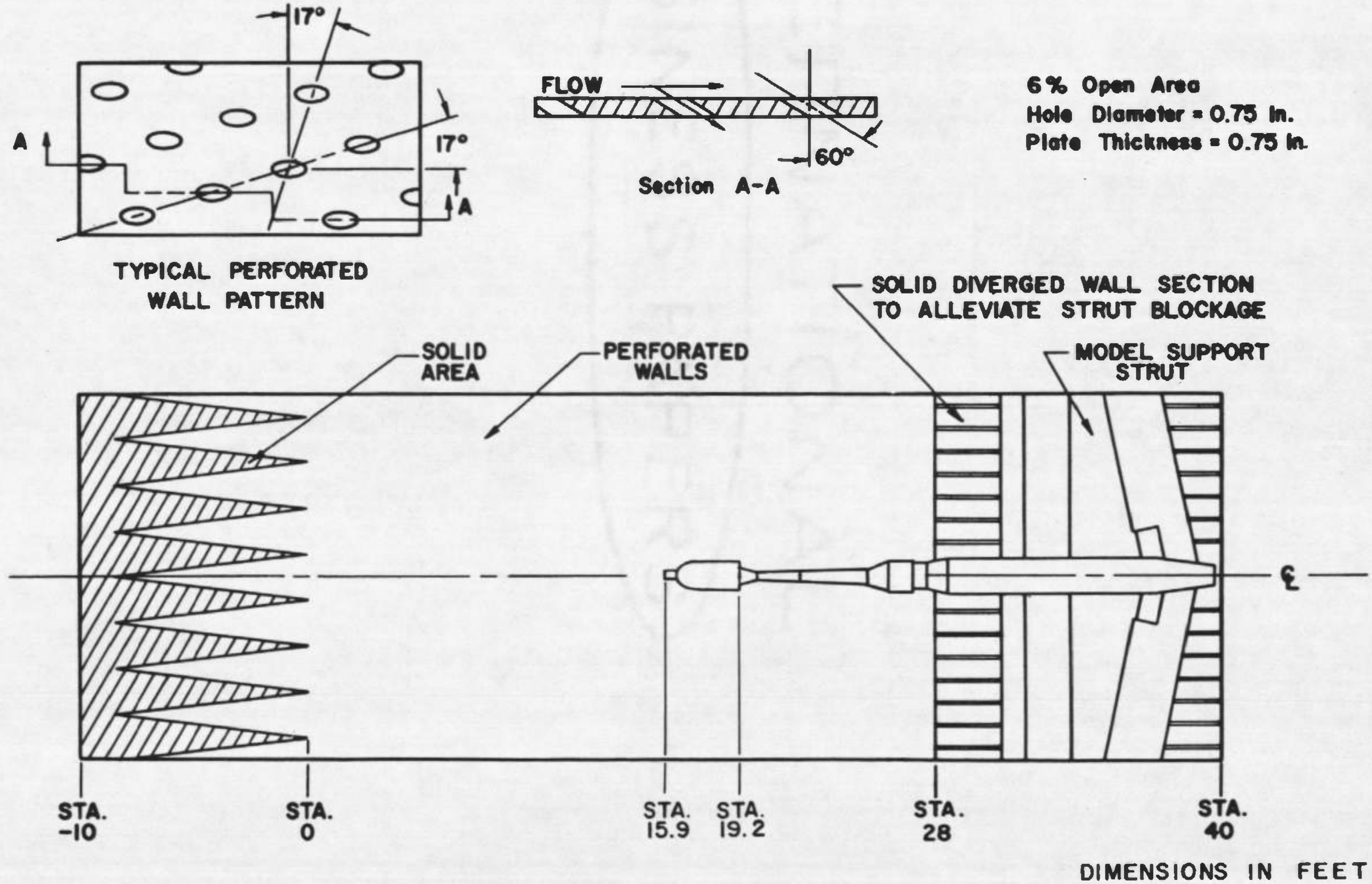

Figure 1. Sketch of model in 16T test section.

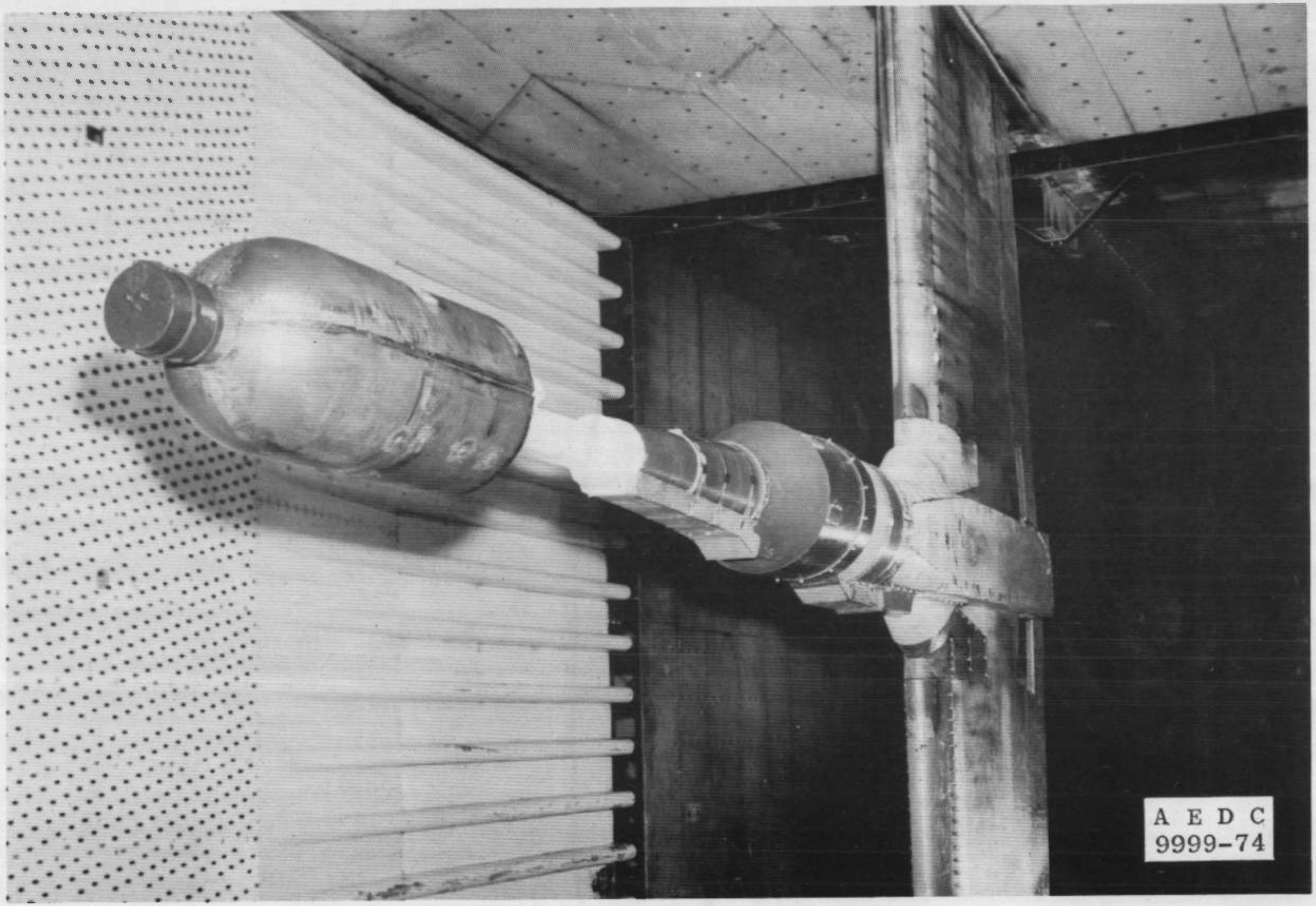

Figure 2. Installation photograph.

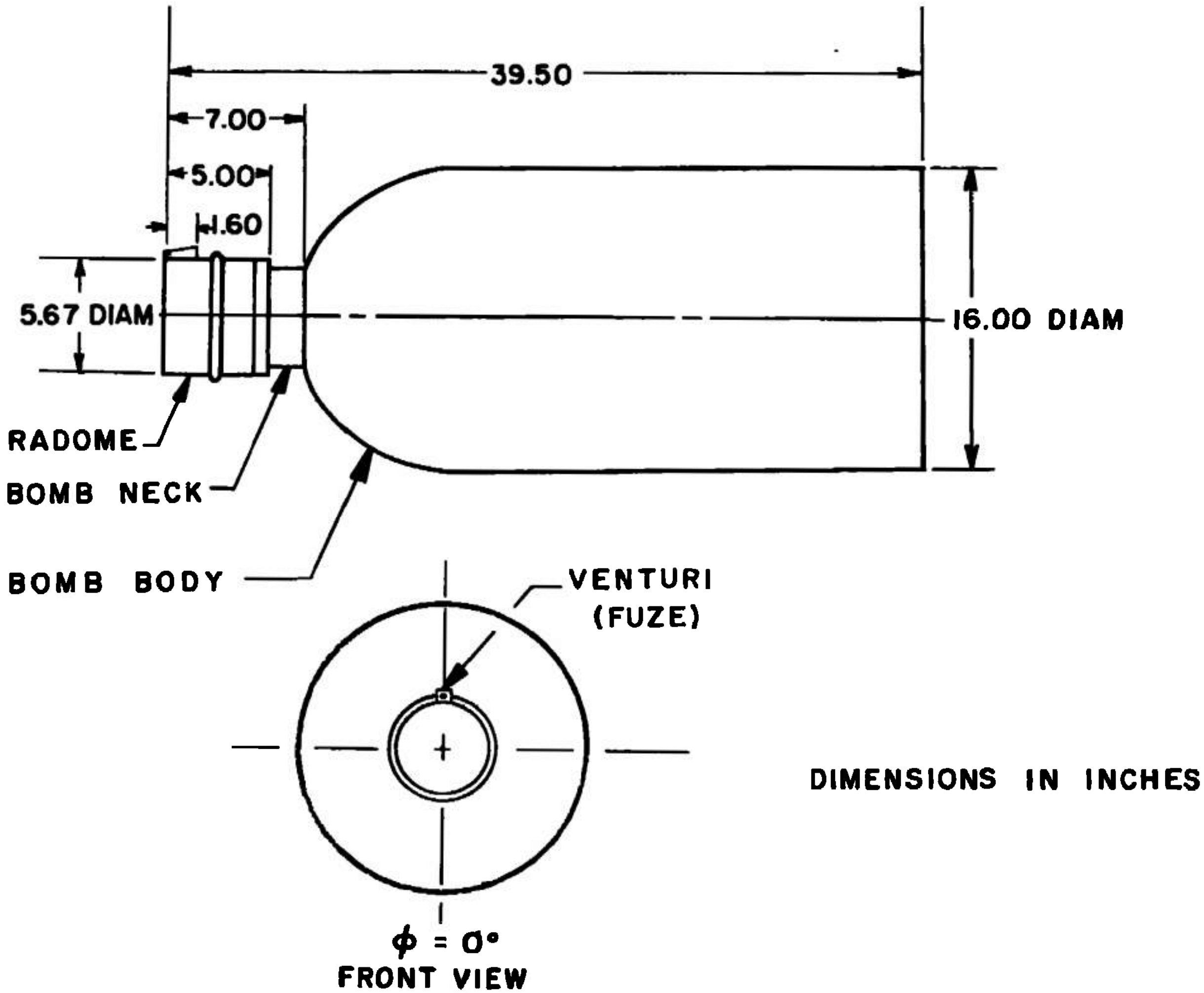

a. Model
Figure 3. Dimensional sketches.

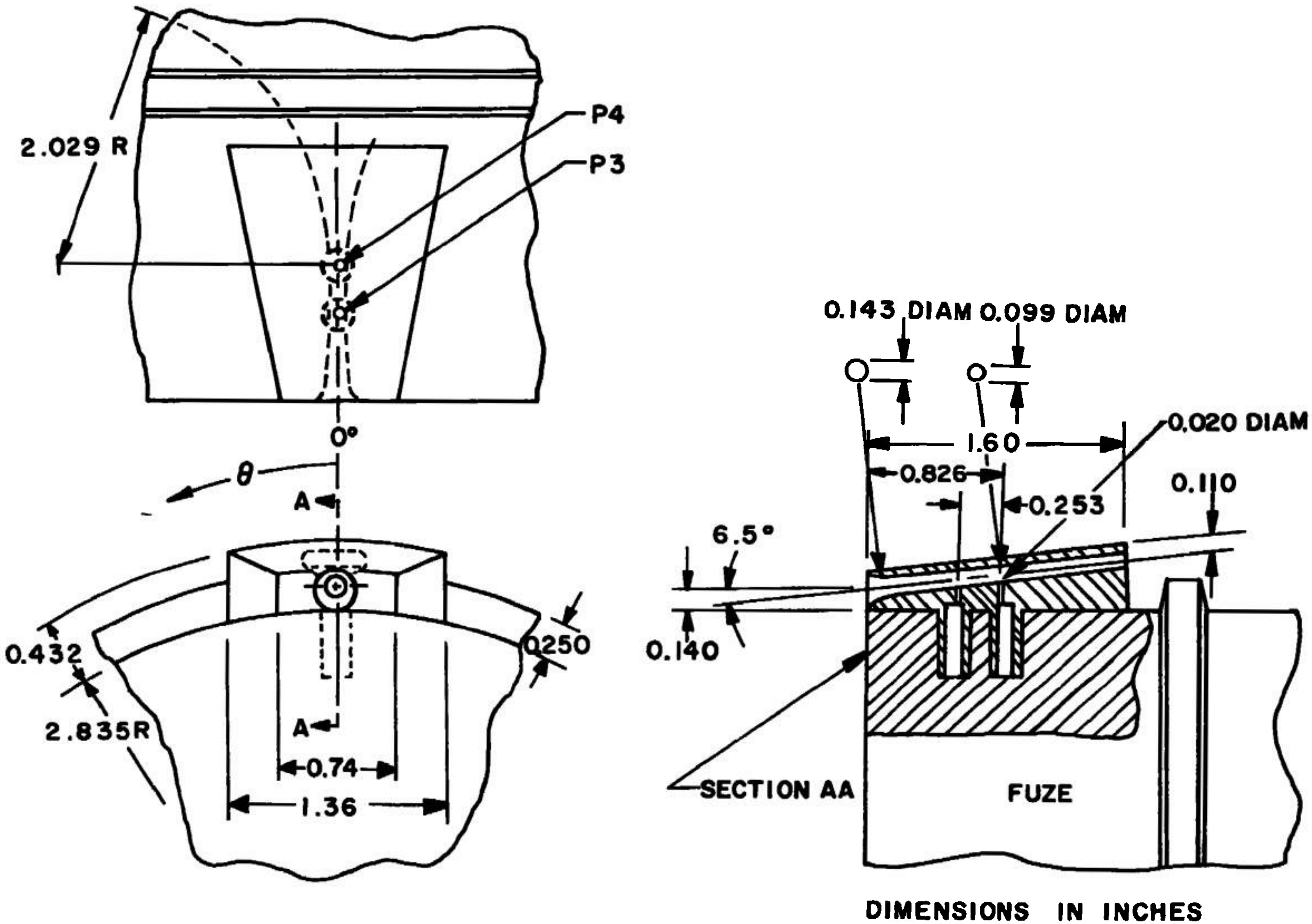

b. Venturi
Figure 3. Concluded.

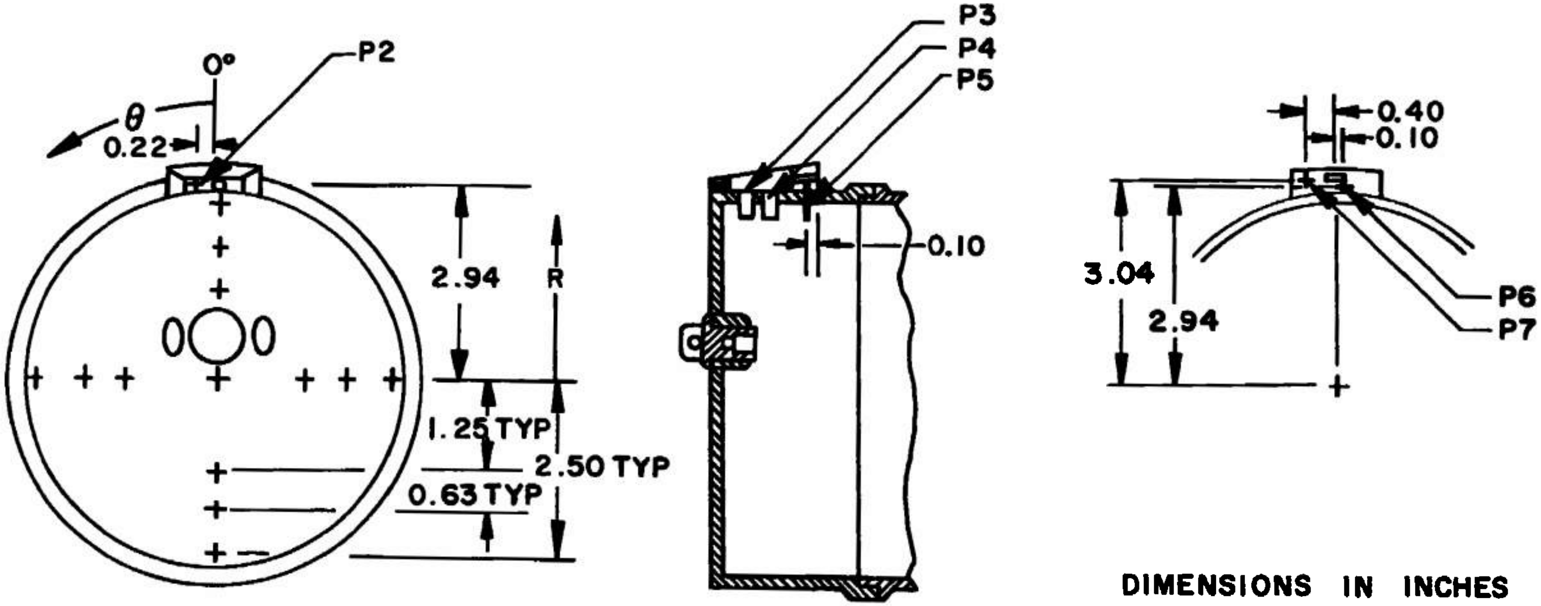

PRESSURE ORIFICE LOCATIONS

θ	R = 0.00	1.25	1.88	2.50
0	P1	P100	P101	102
-90	——	200	201	202
180	——	300	301	302
90	——	400	401	402

Figure 4. Sketch and location of radome face and fuze region pressure orifices.

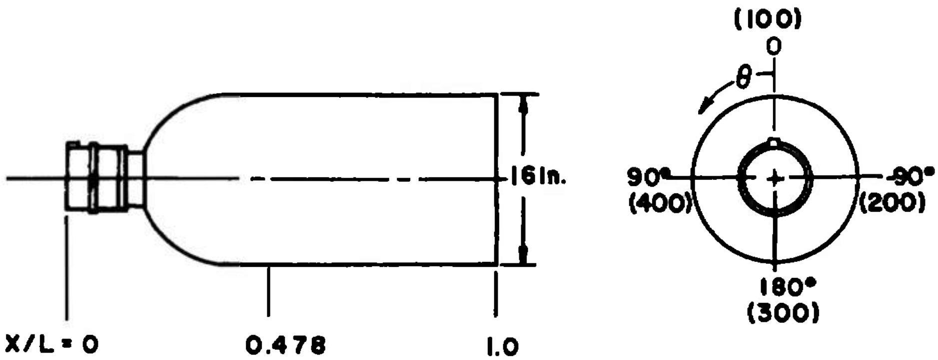

PRESSURE ORIFICE LOCATIONS

	X/L	θ = 0 deg	-90 deg	180 deg	90 deg
RADOME	0.014	—	P 203	P 303	P 403
	0.019	—	204	304	404
	0.026	—	205	305	405
	0.033	—	206	306	406
	0.043	P 103	207	307	407
	0.062	104	208	308	408
	0.076	105	209	309	409
	0.086	106	210	—	410
	0.100	—	—	—	411
BOMB NECK	0.132	107	211	310	412
	0.143	108	212	311	413
	0.157	109	213	312	414
	0.169	110	214	313	415
BOMB BODY	0.181	111	215	314	416
	0.201	112	216	315	417
	0.227	113	217	316	418
	0.258	114	218	317	419
	0.292	115	219	218	420
	0.325	116	220	319	421
	0.363	117	221	320	422
	0.402	118	222	321	423
	0.440	119	223	322	424
	0.478	120	224	323	425

Figure 5. Location of radome and bomb body pressure orifices.

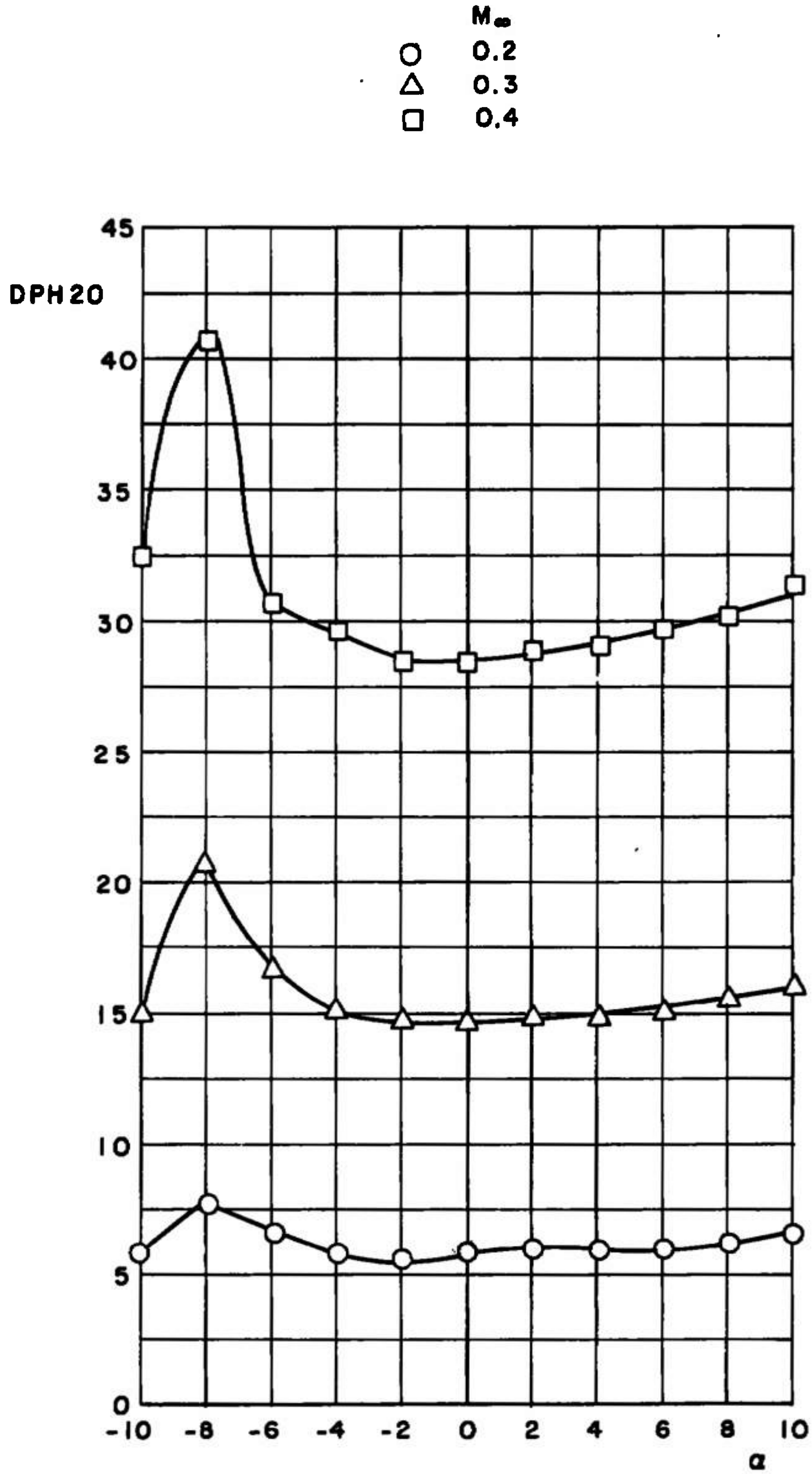

Figure 6. Variation of pressure differential with angle of attack.

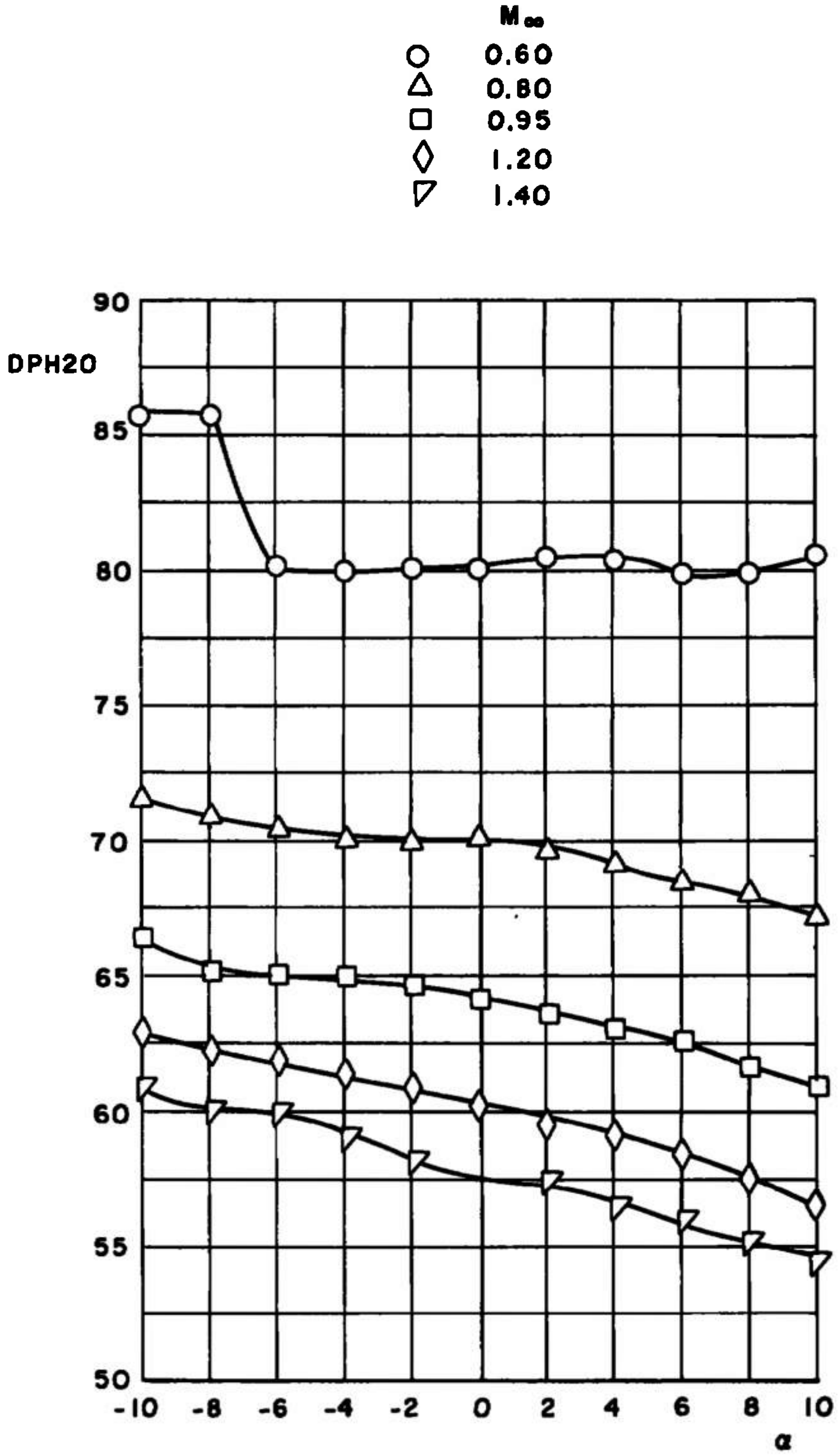

Figure 6. Concluded.

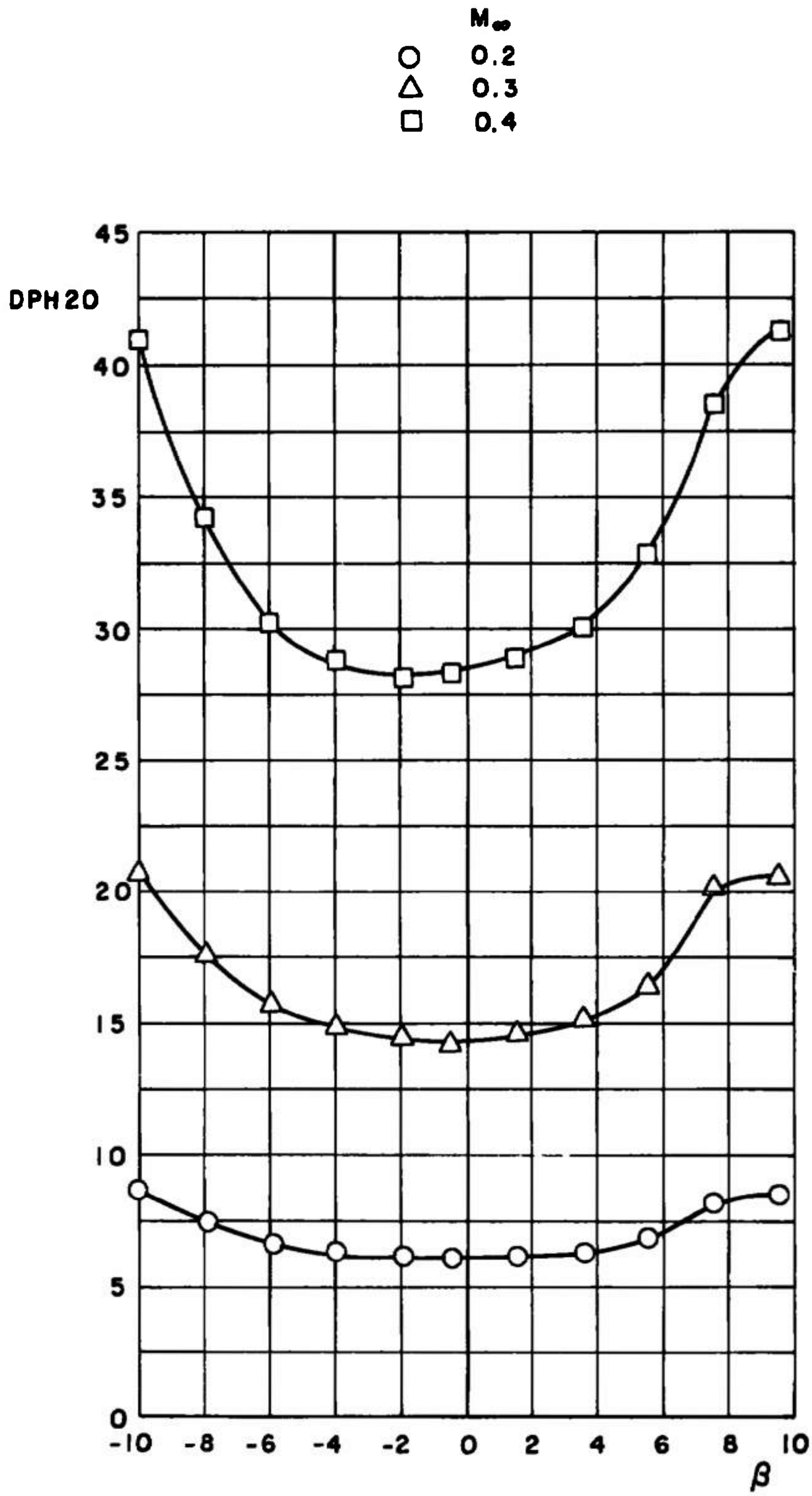

Figure 7. Variation of pressure differential with beta angle.

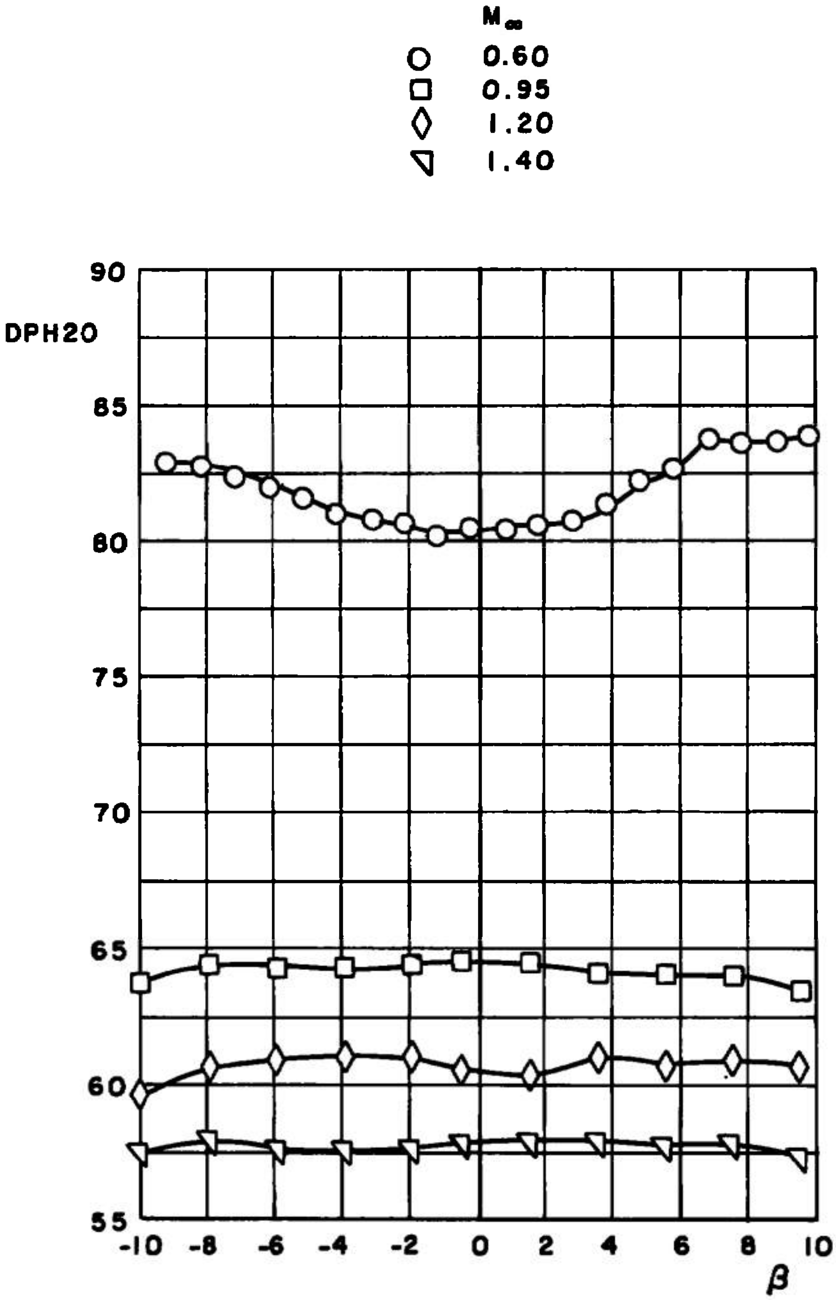

Figure 7. Concluded.

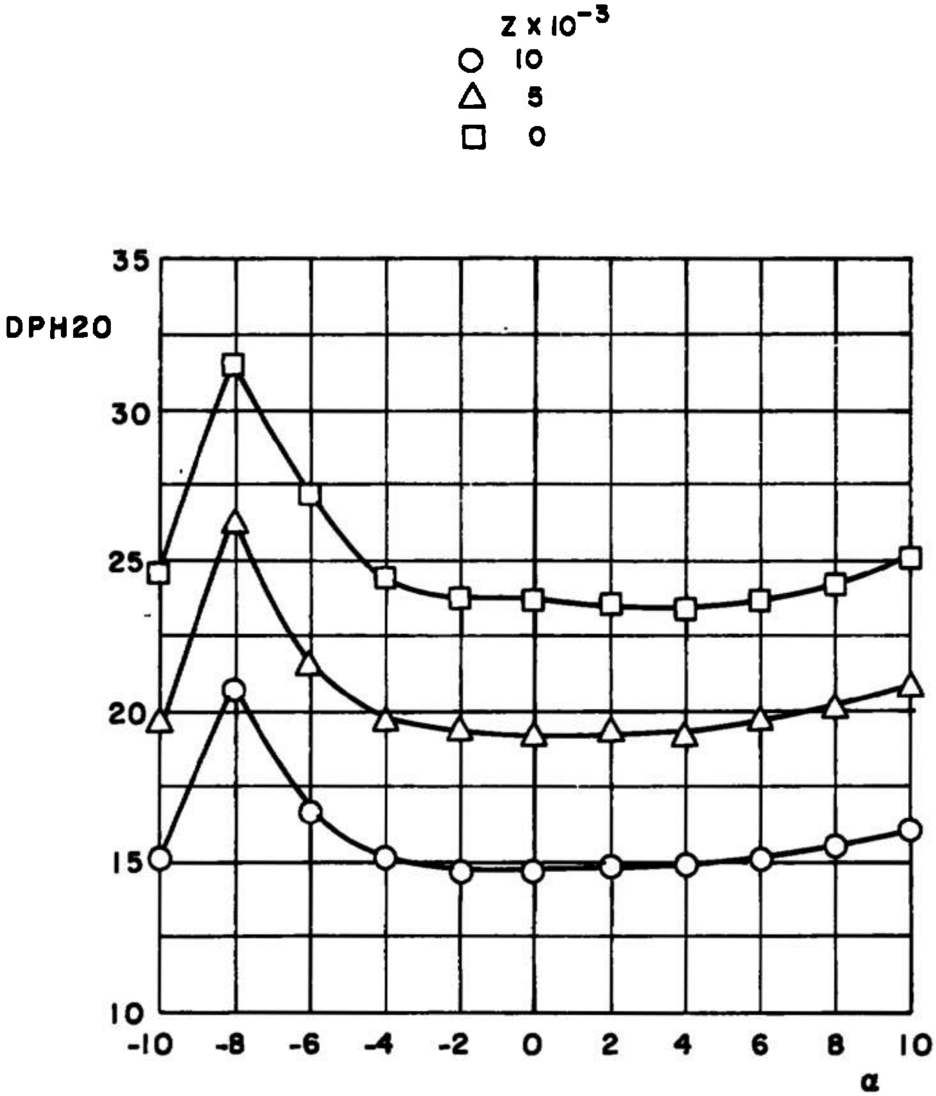

Figure 8. Influence of pressure altitude and angle of attack on the fuze pressure differential at $M_\infty = 0.30$.

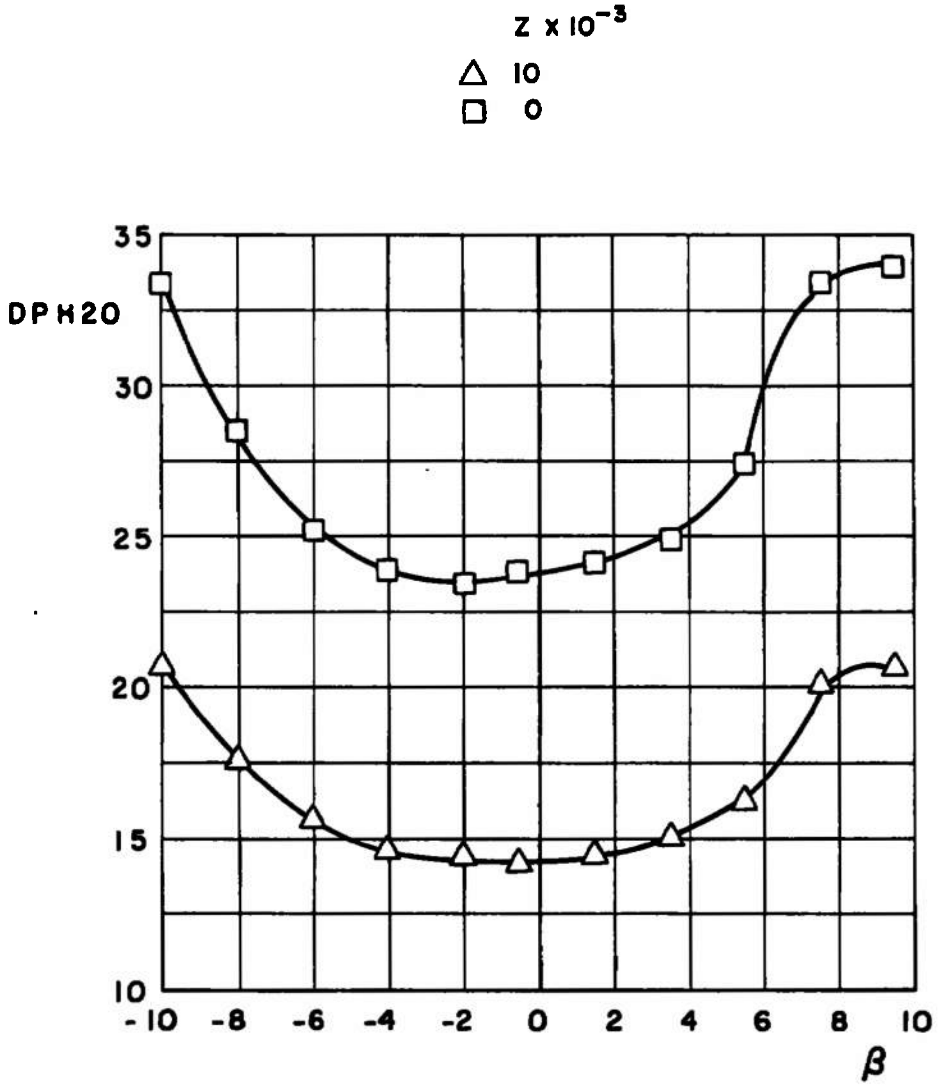

Figure 9. Influence of pressure altitude and beta angle on pressure differential at M_∞ = 0.30.

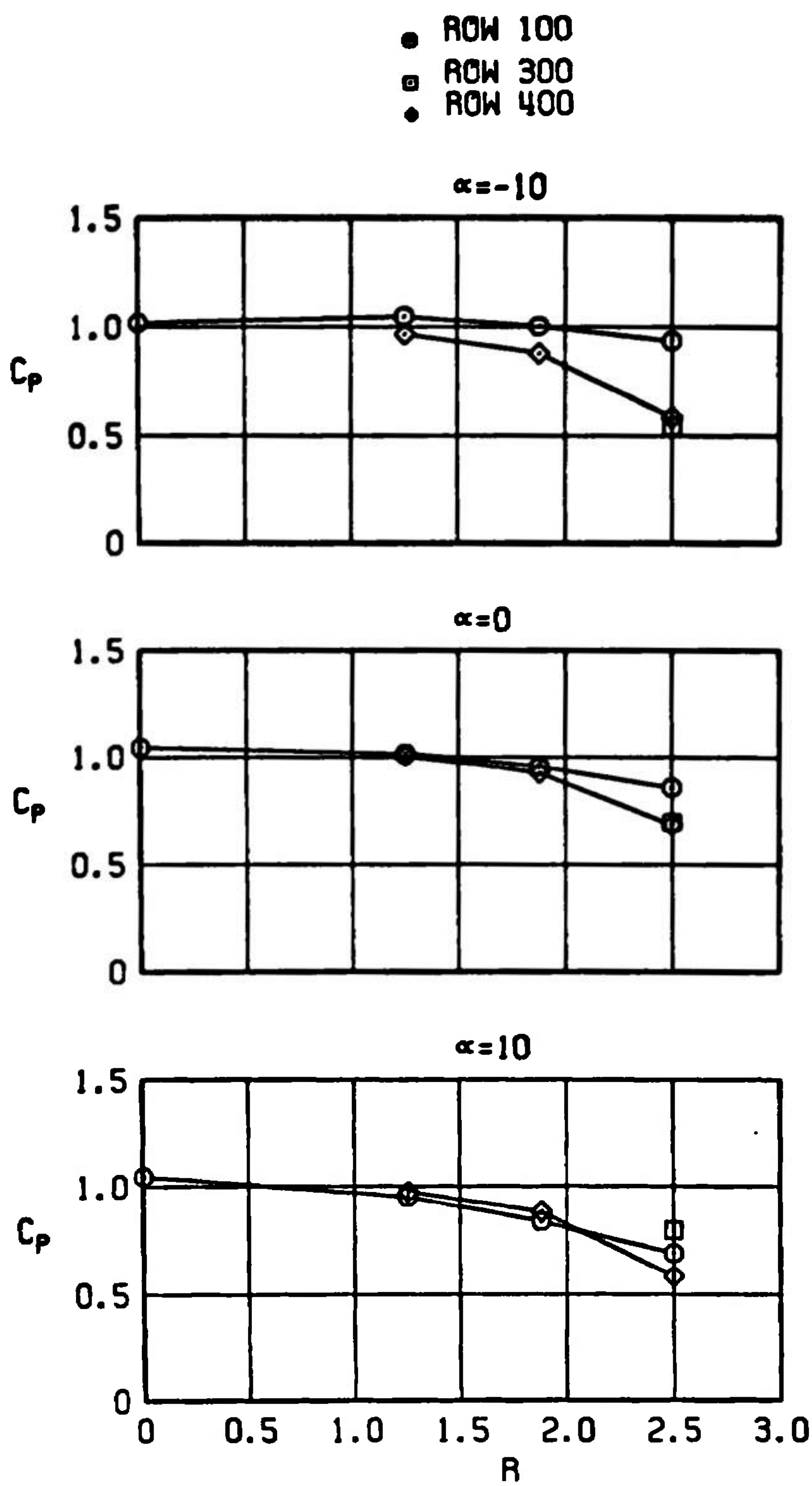

a. $M_\infty = 0.20$

Figure 10. Effect of angle of attack on the pressure profiles on the radome face.

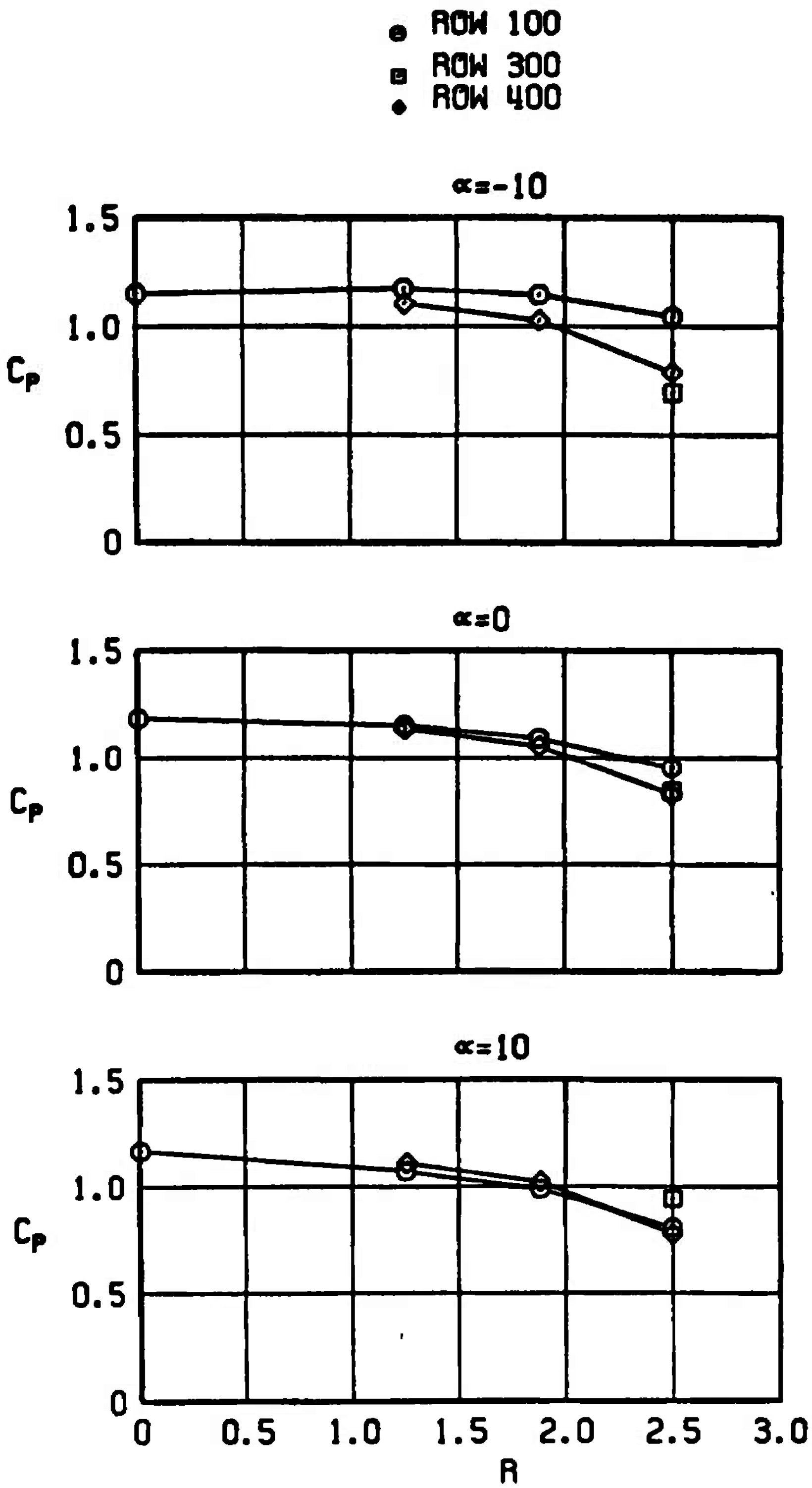

b. $M_\infty = 0.80$
Figure 10. Continued.

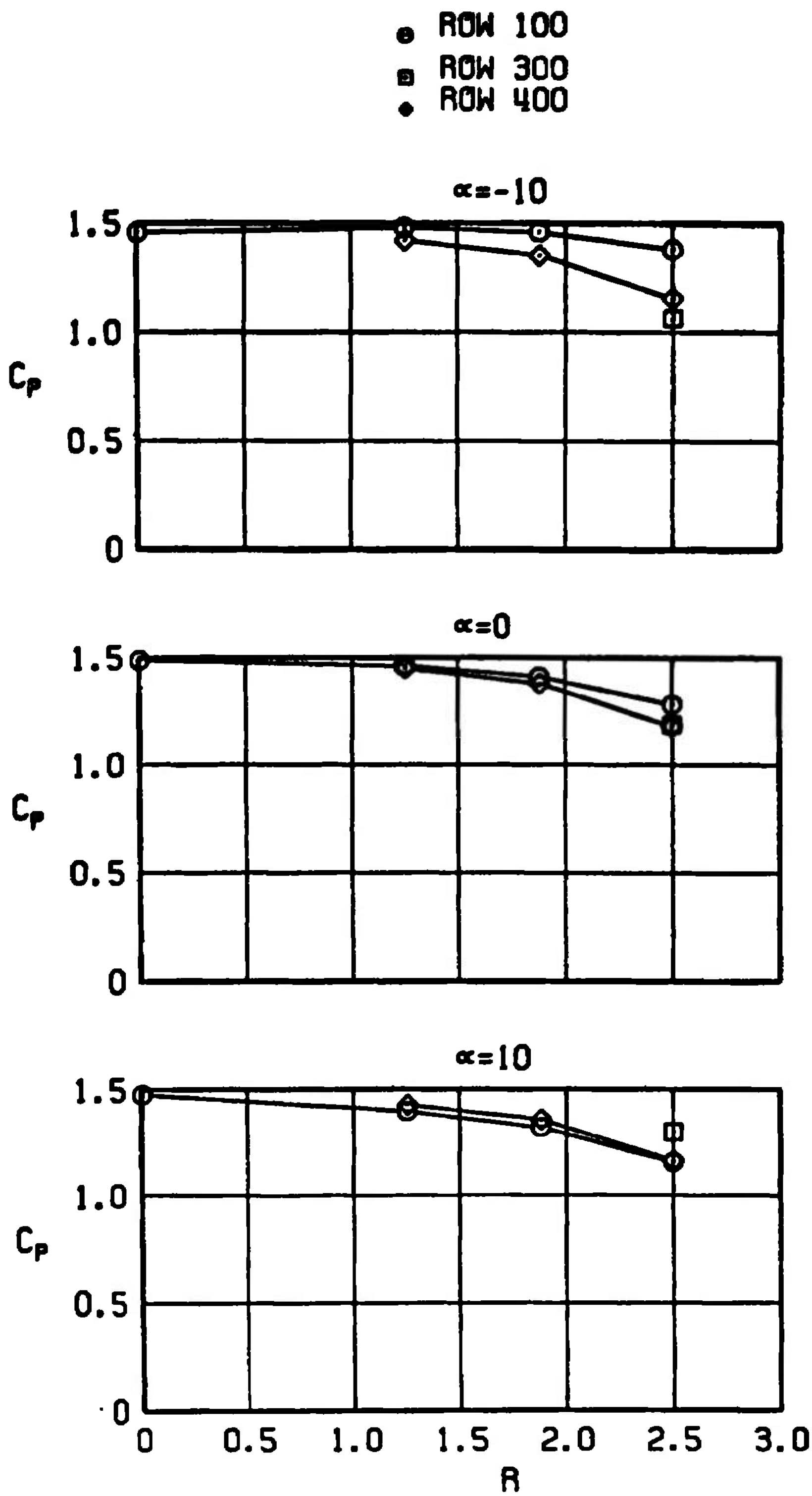

c. M_∞ = 1.40
Figure 10. Concluded.

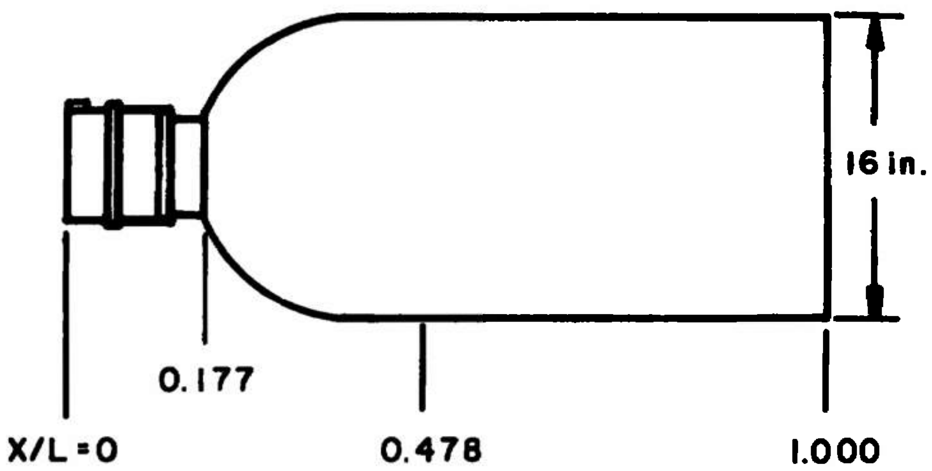

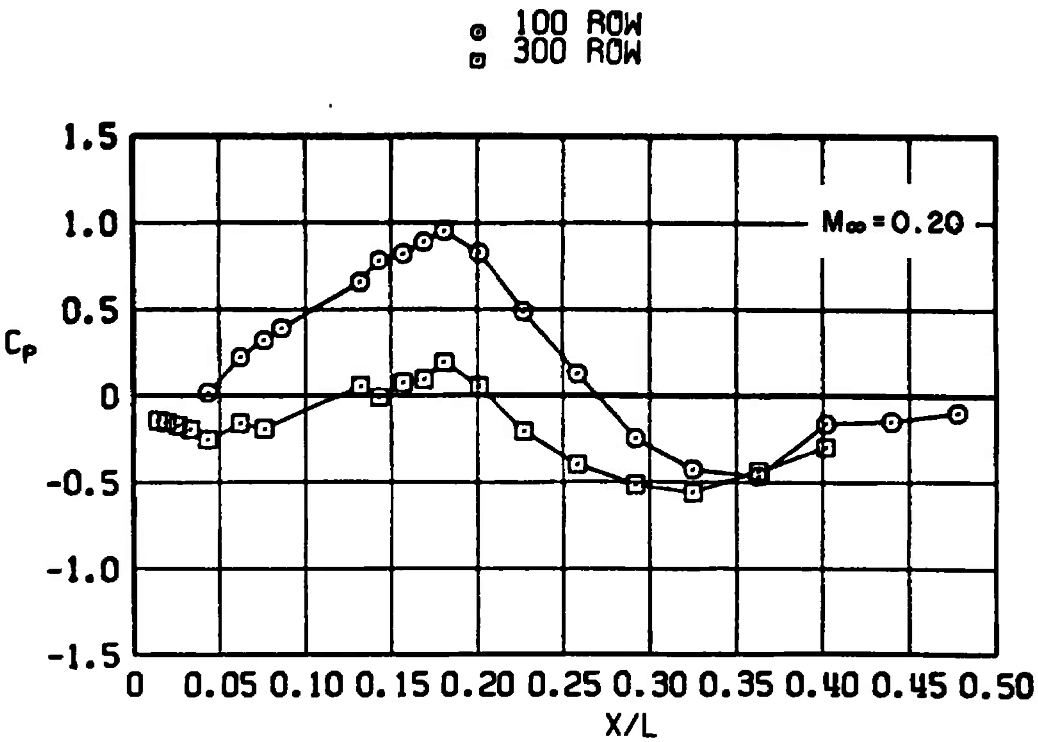

Figure 11. Pressure profiles along the top and bottom runs of the radome-bomb body at -10-deg angle of attack.

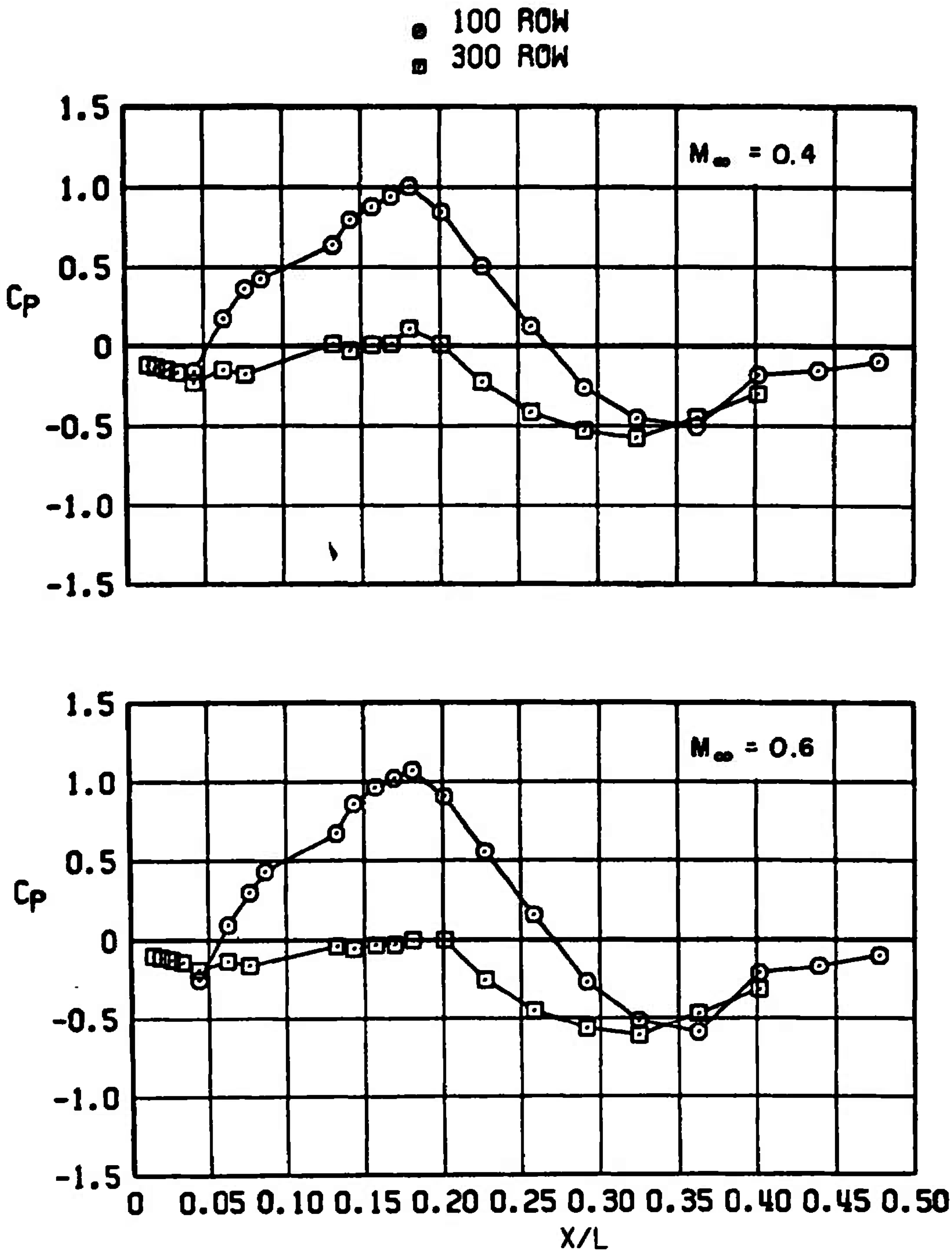

Figure 11. Continued.

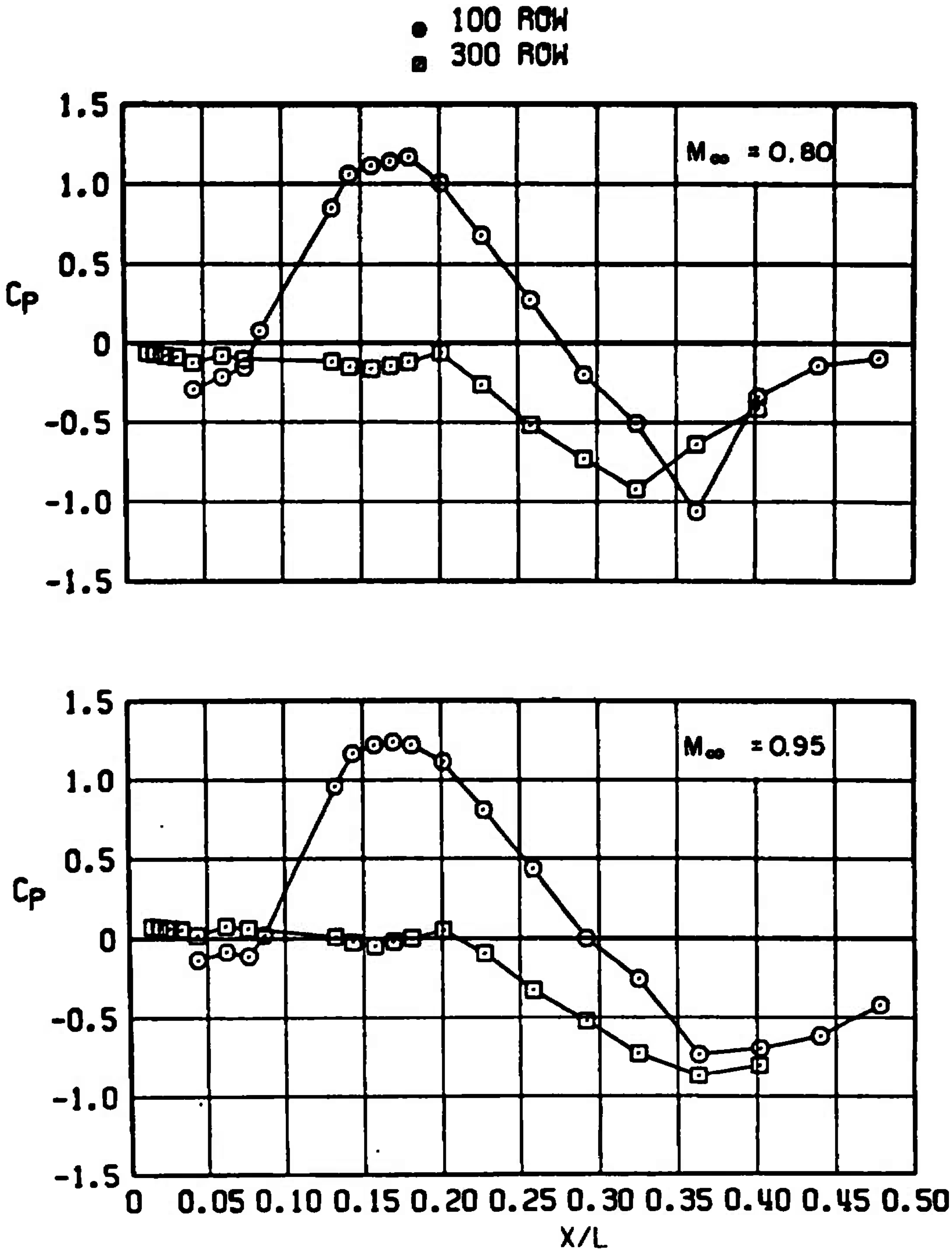

Figure 11. Continued.

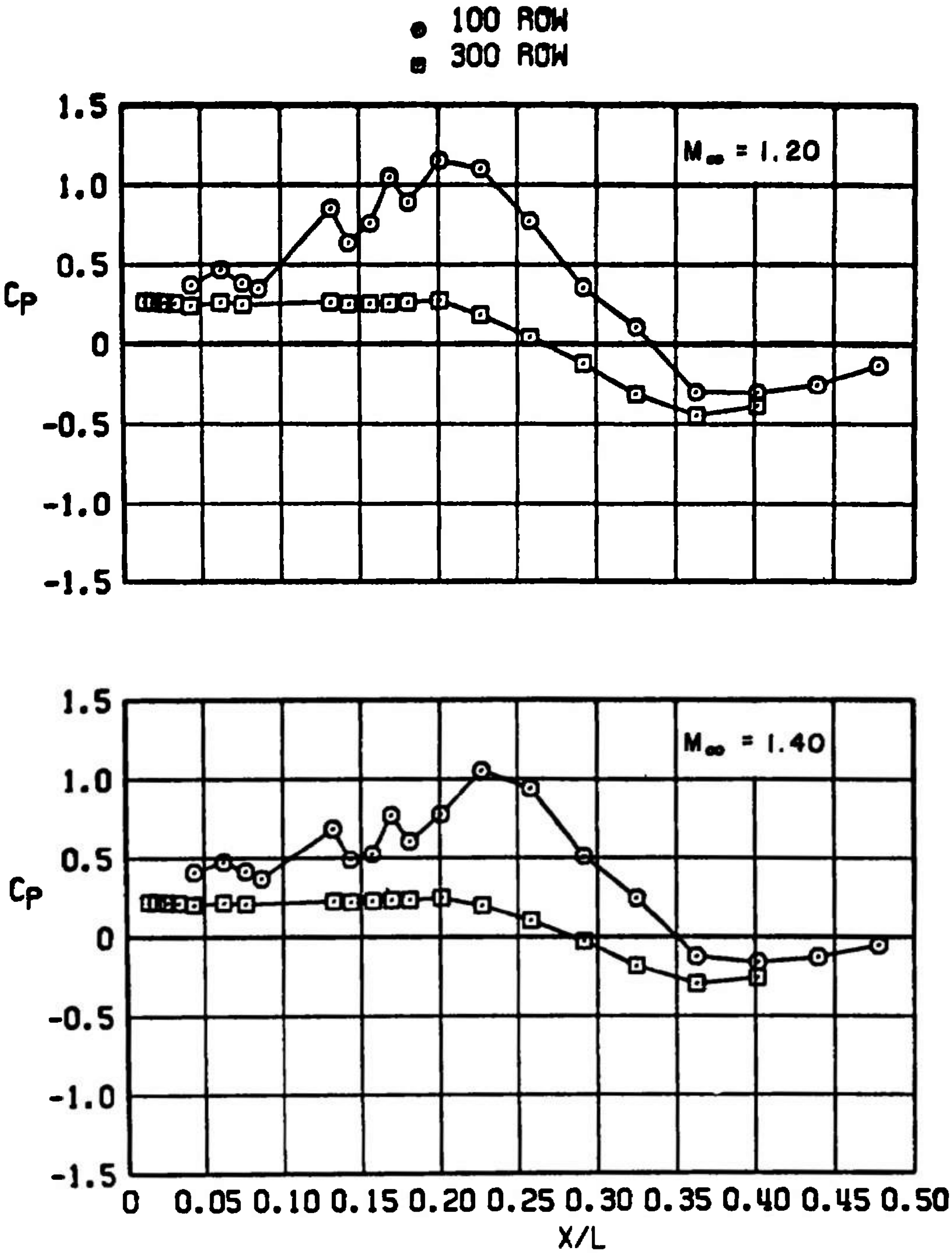

Figure 11. Concluded.

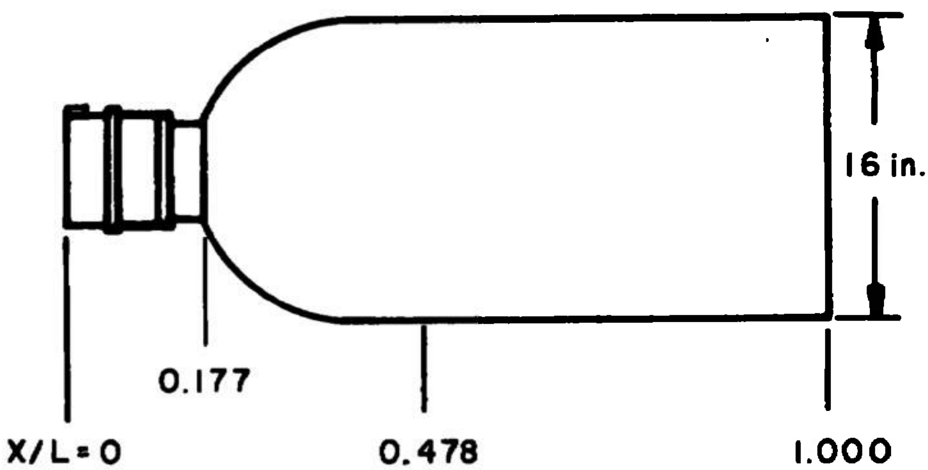

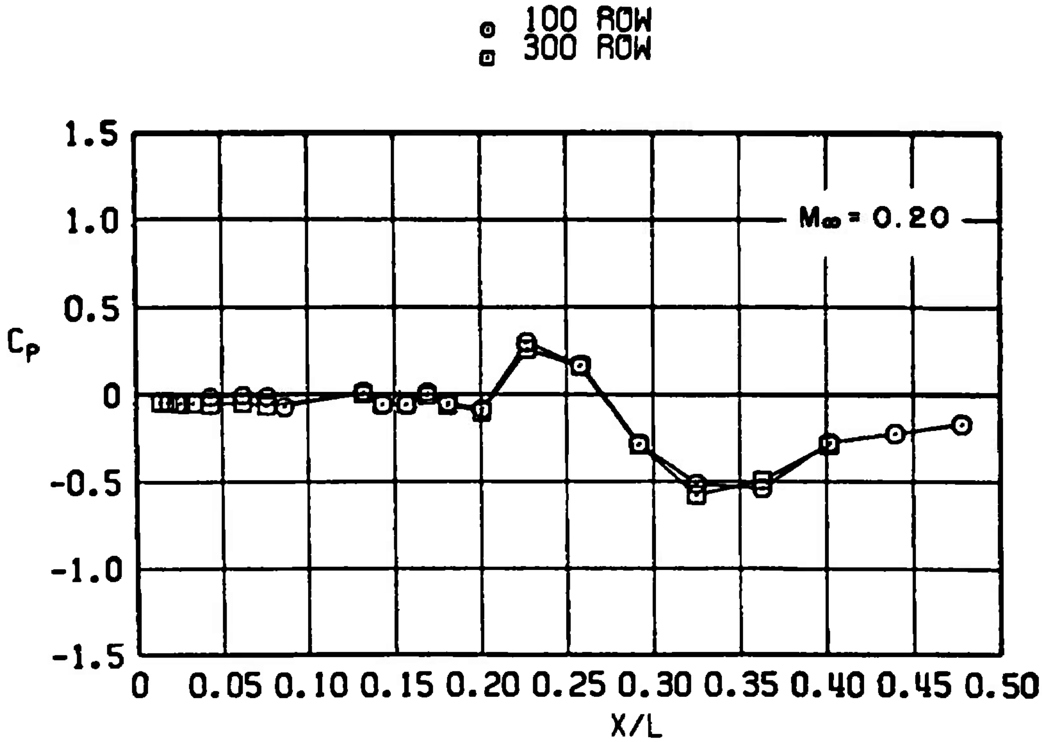

Figure 12. Pressure profiles along the radome-bomb body at α = 0.

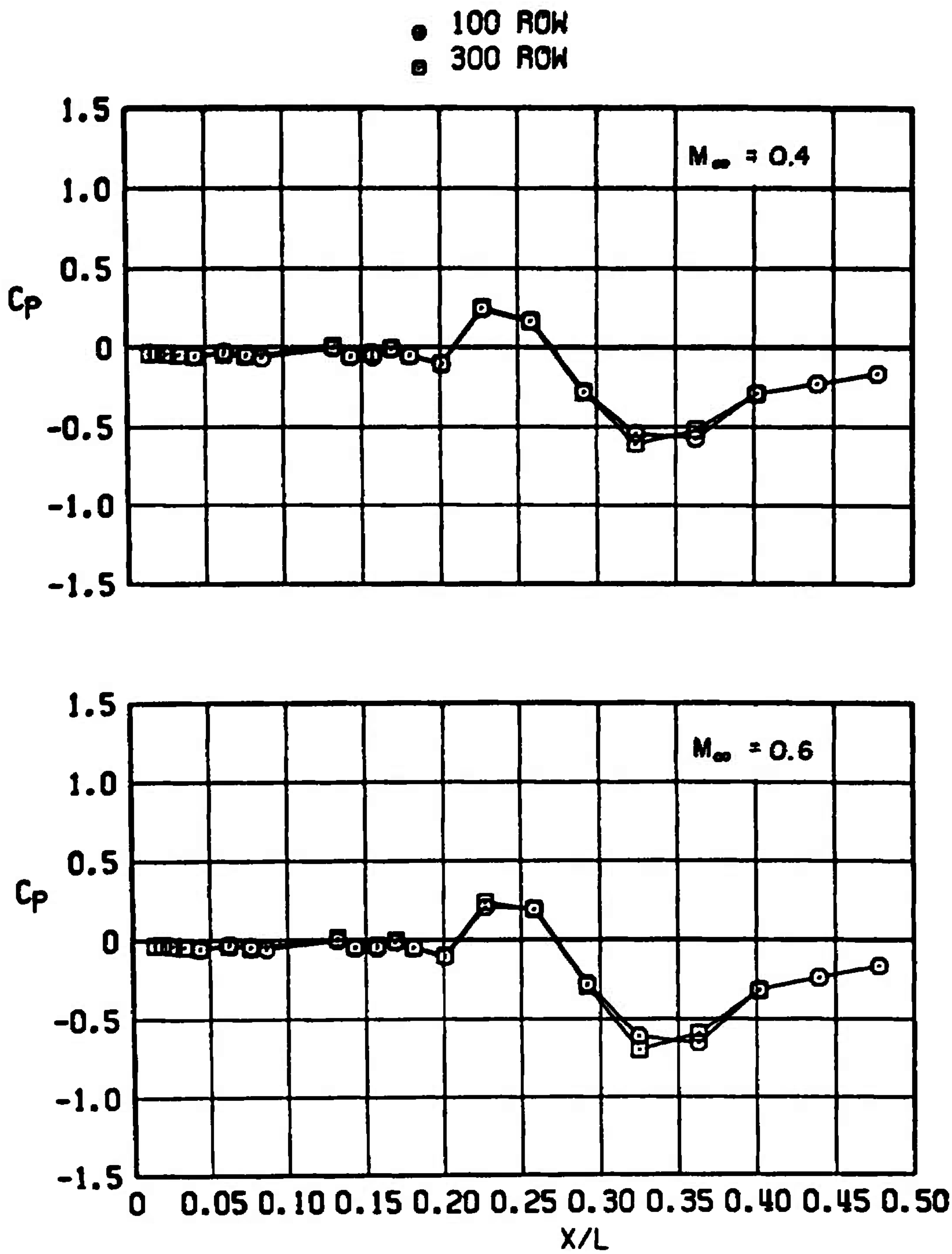

Figure 12. Continued.

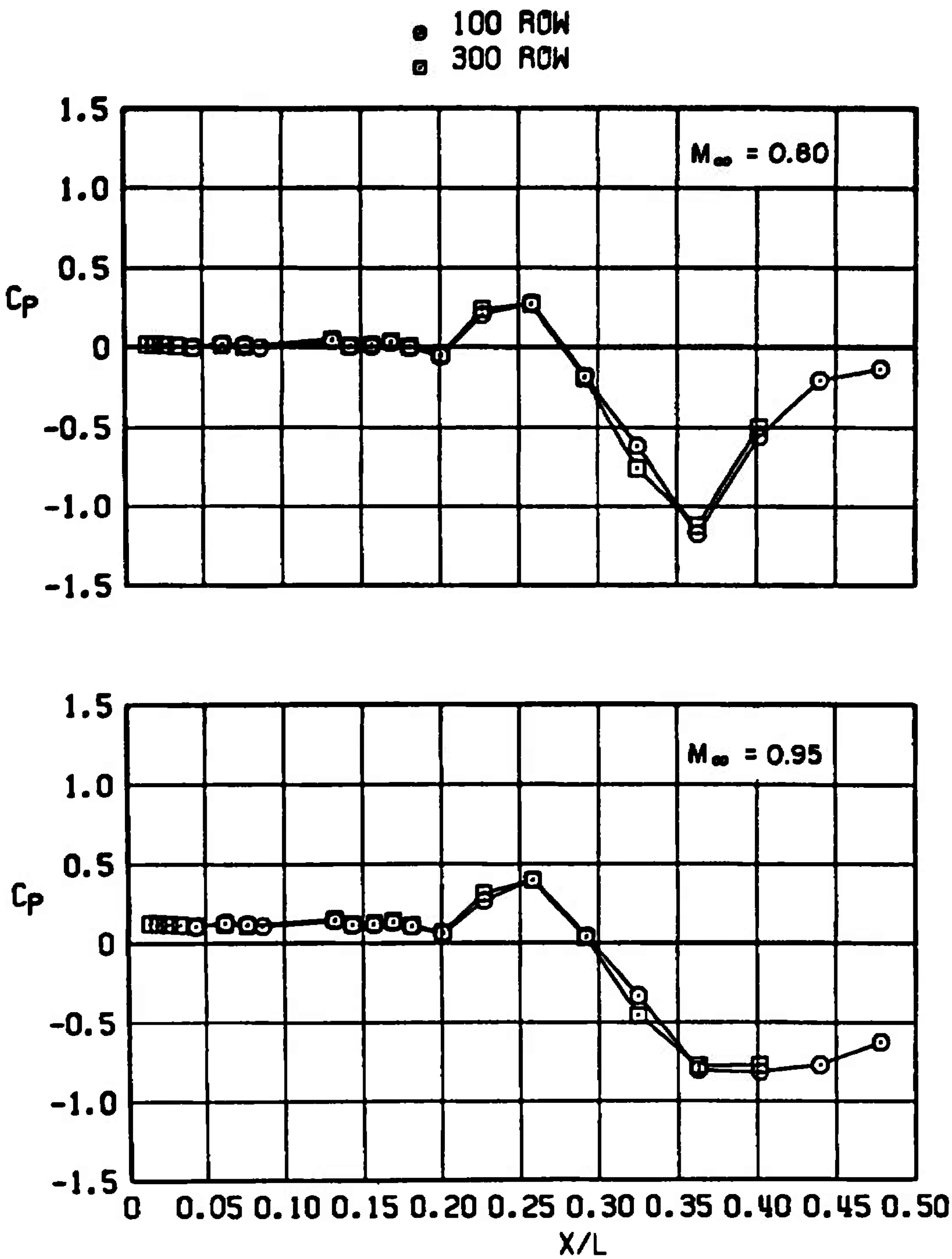

Figure 12. Continued.

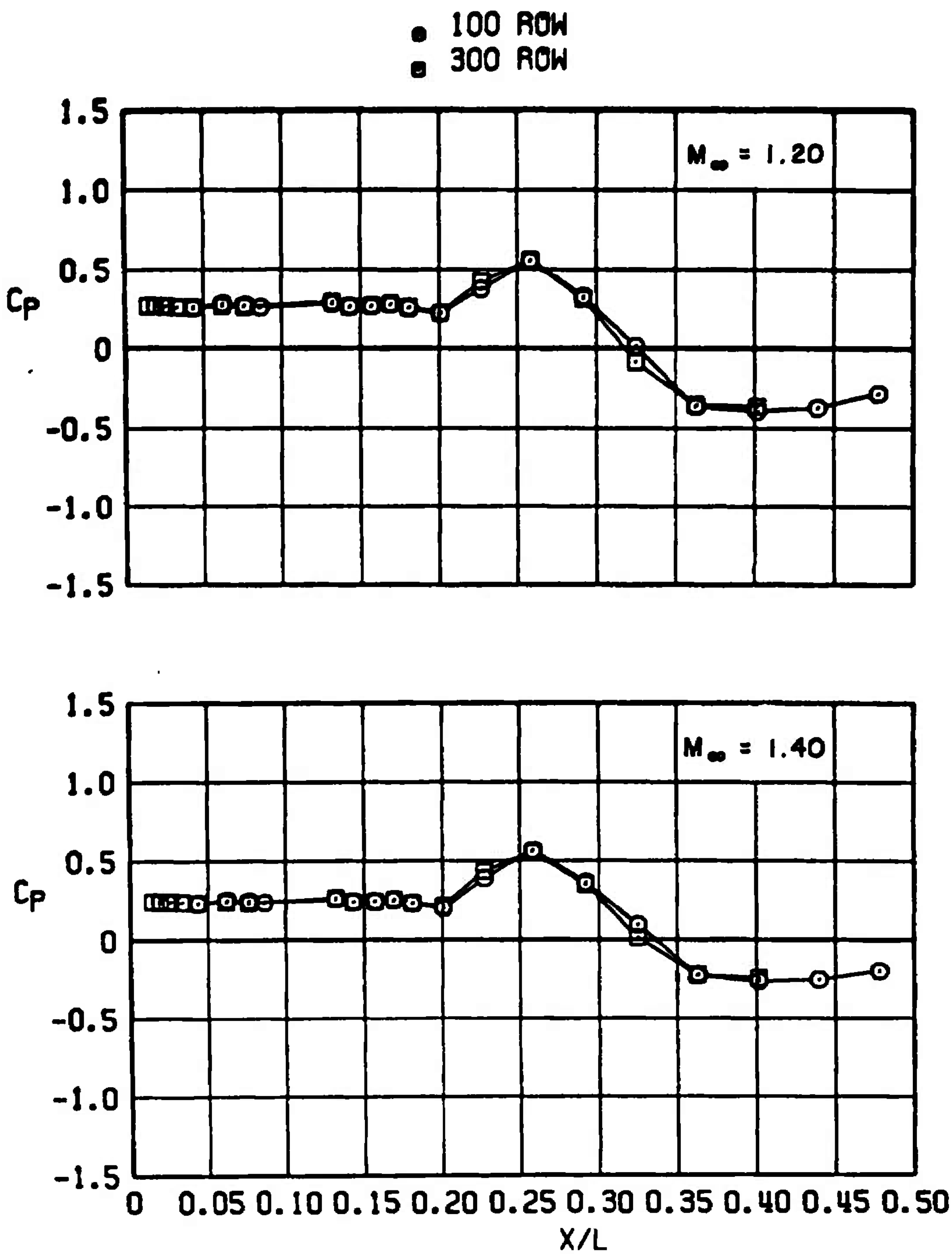

Figure 12. Concluded.

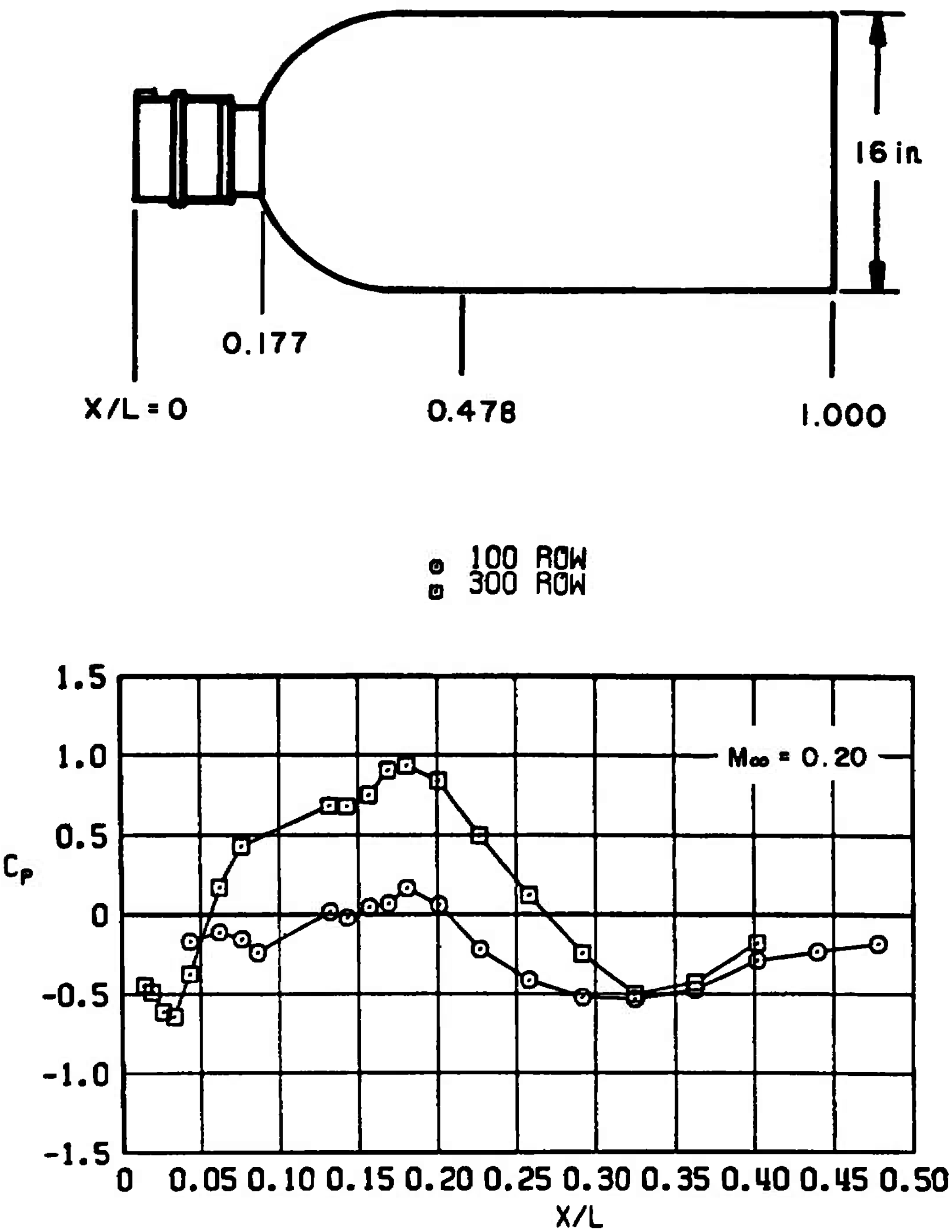

Figure 13. Pressure profiles along the radome-bomb body at α = 10 deg.

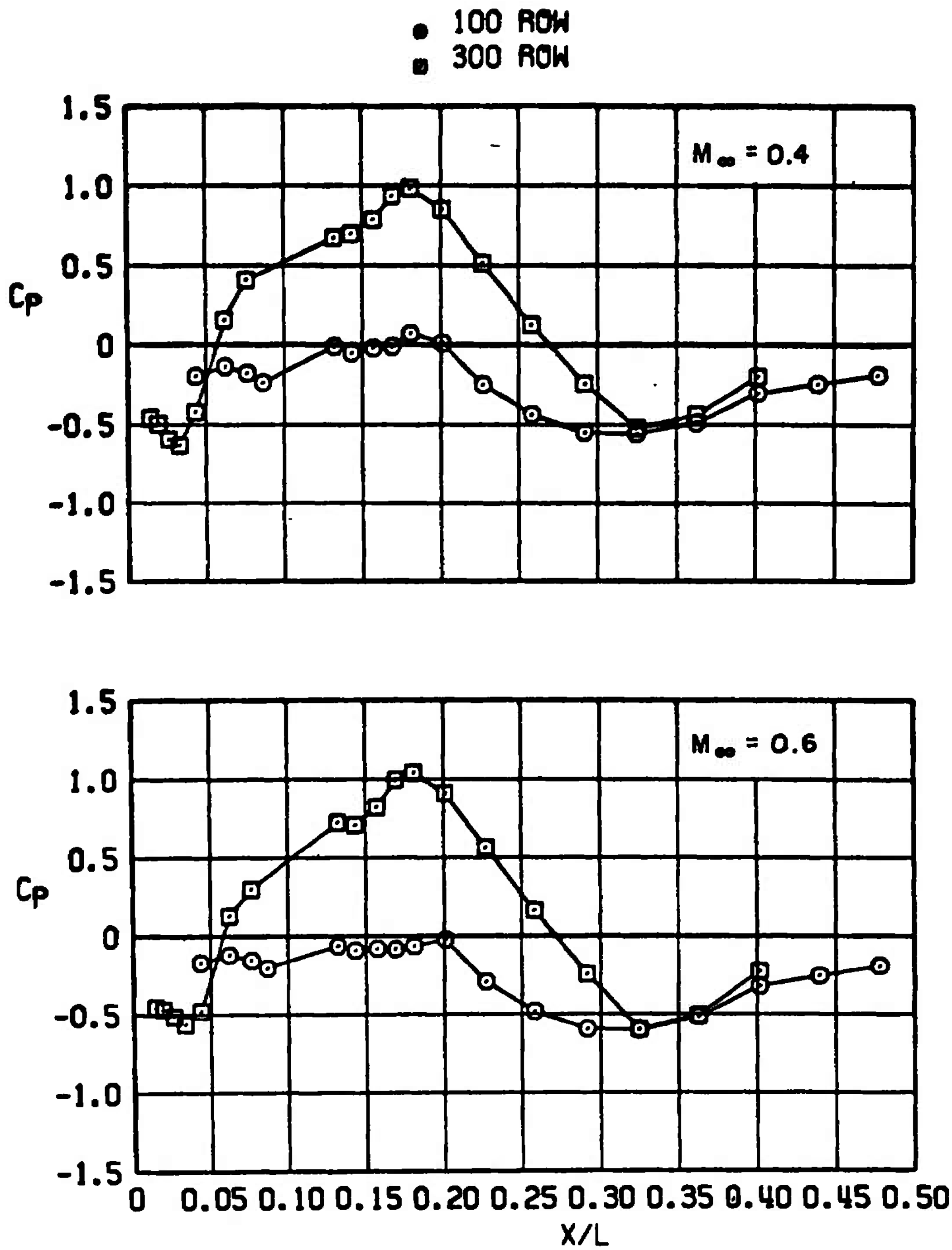

Figure 13. Continued.

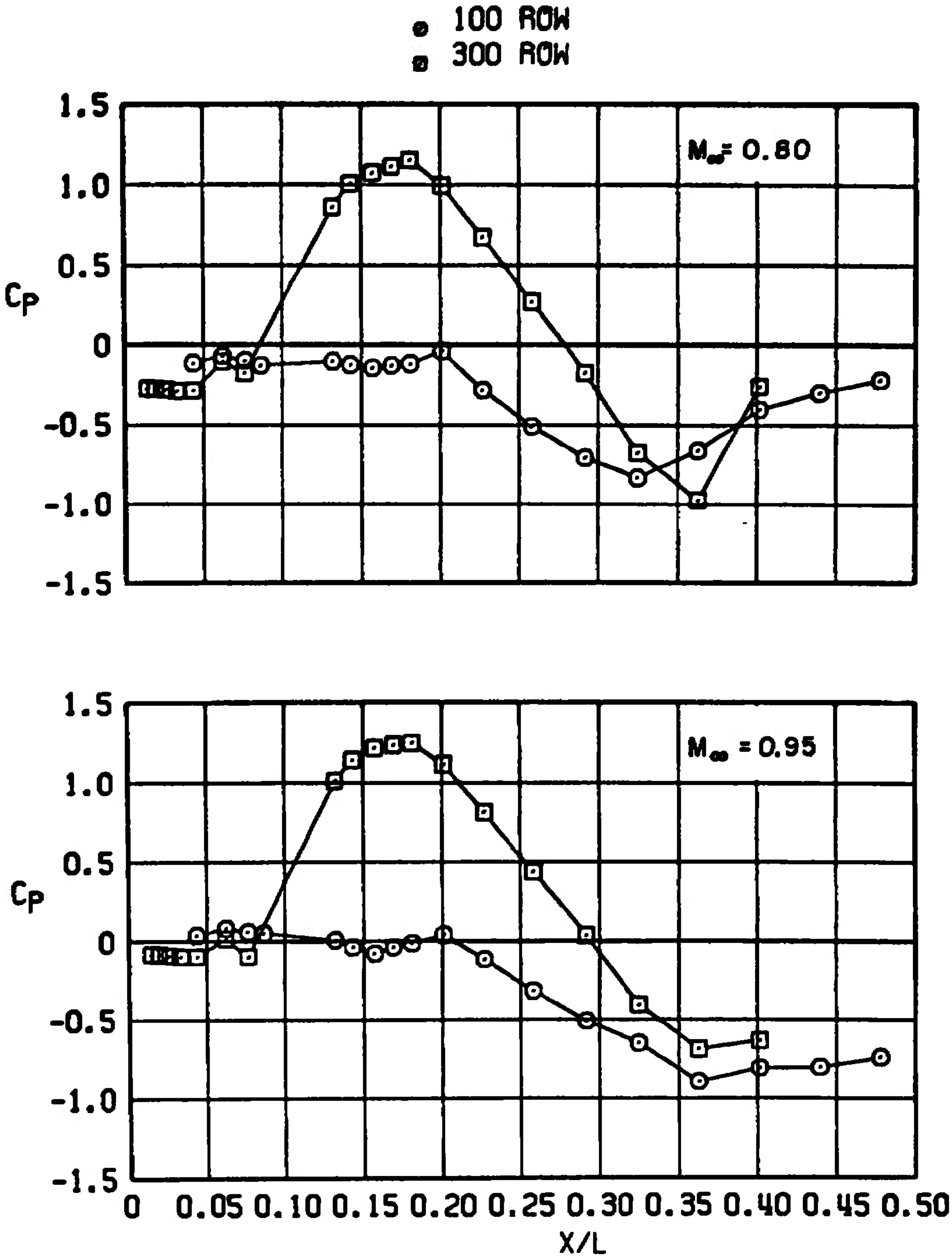

Figure 13. Continued.

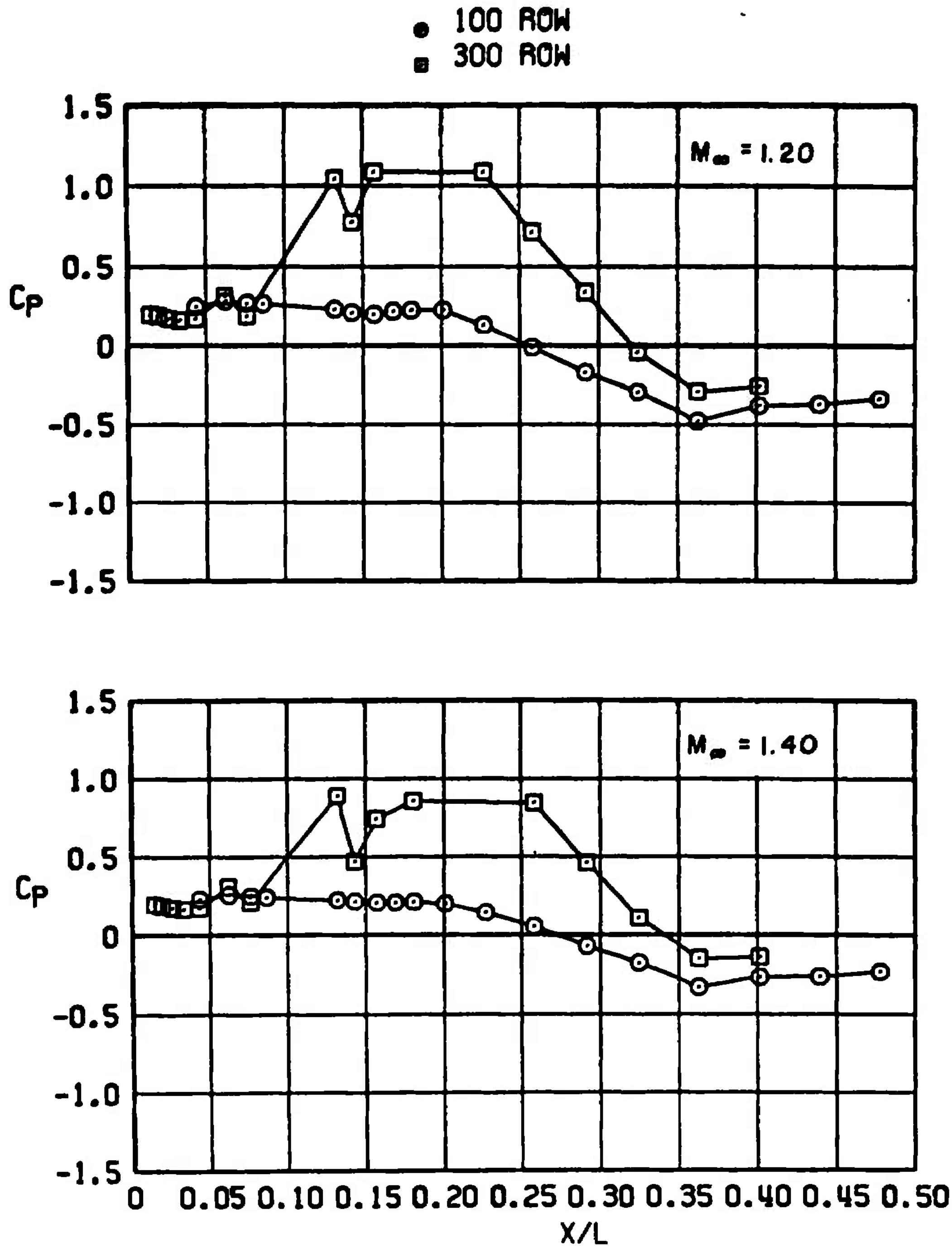

Figure 13. Concluded.

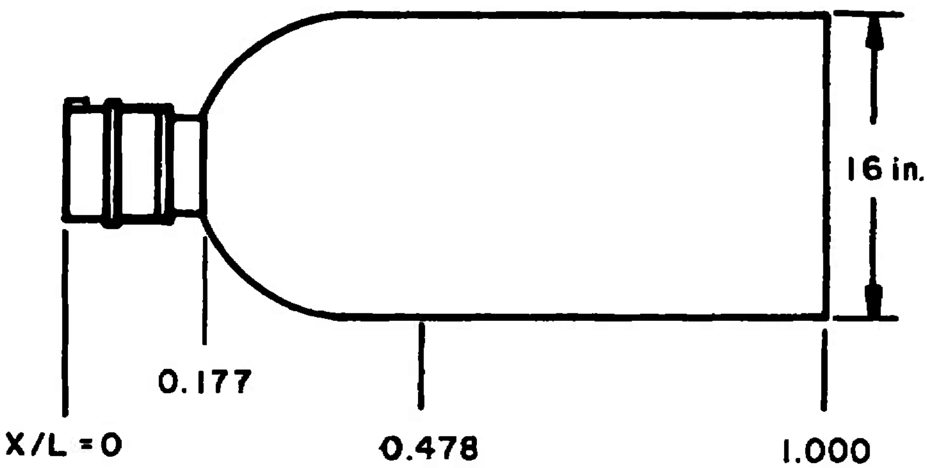

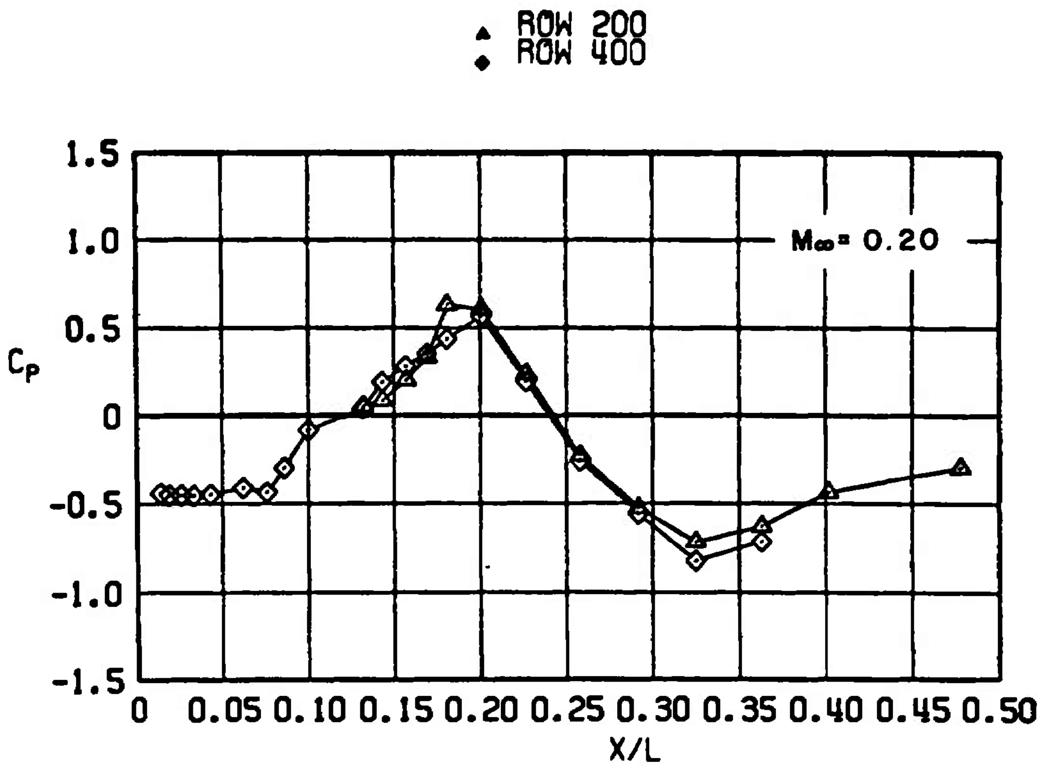

Figure 14. Variation of pressure coefficient along the two side rows of the radome-bomb body at -10-deg angle of attack.

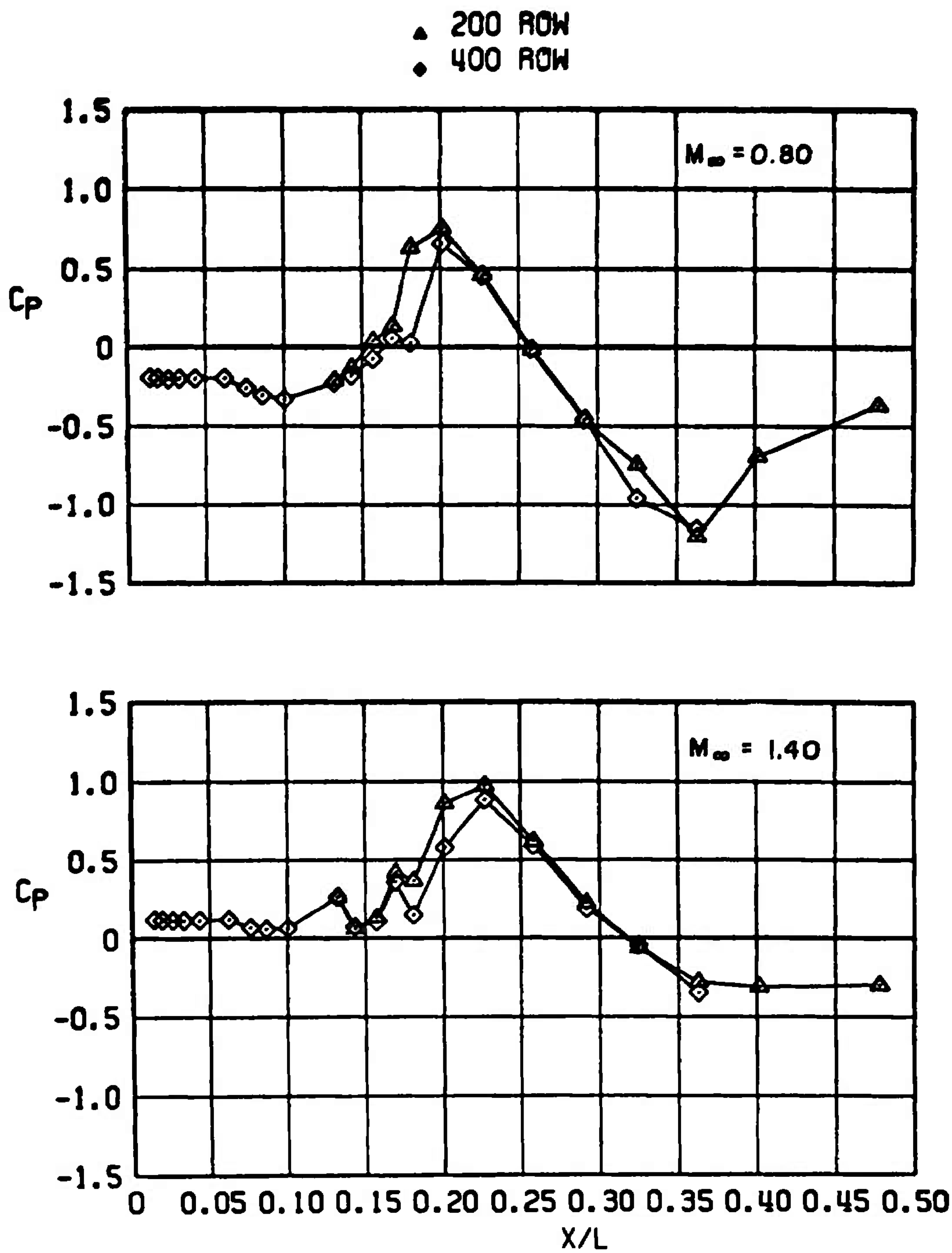

Figure 14. Concluded.

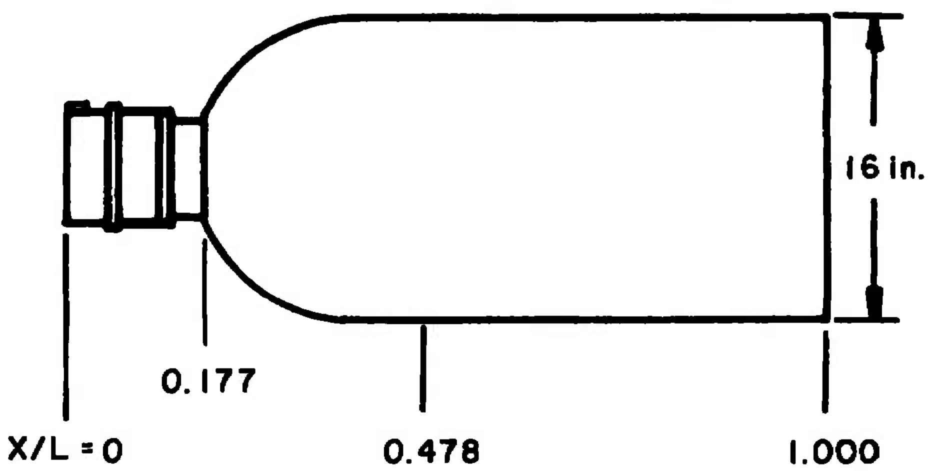

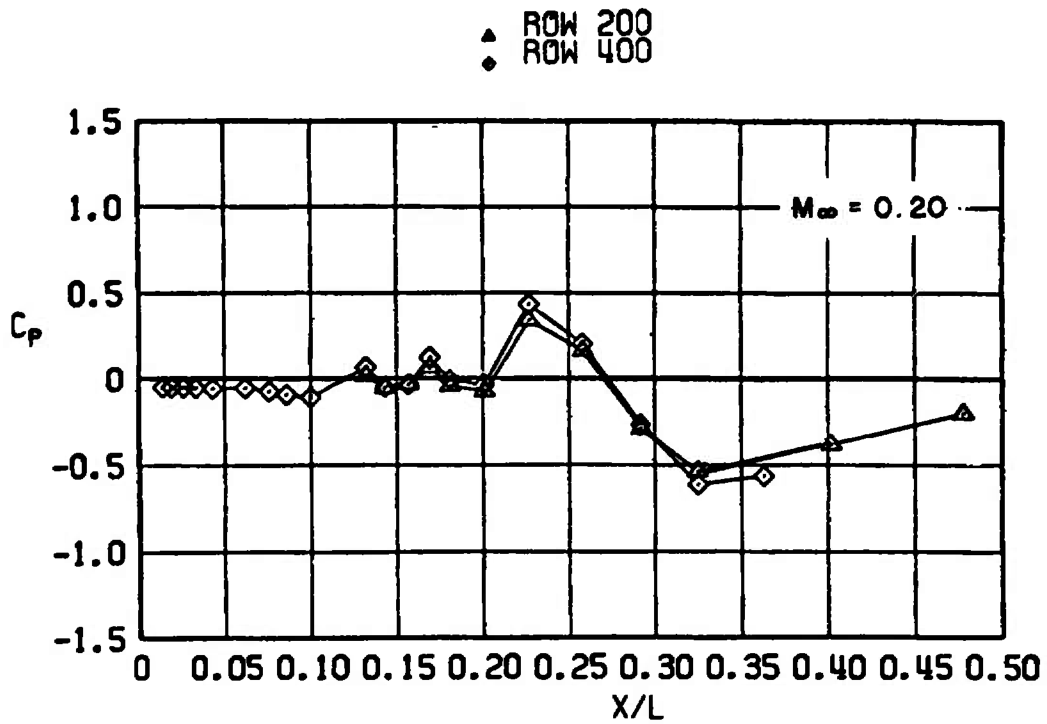

Figure 15. Variation of pressure coefficient along the two side rows of the radome-bomb body at zero angle of attack.

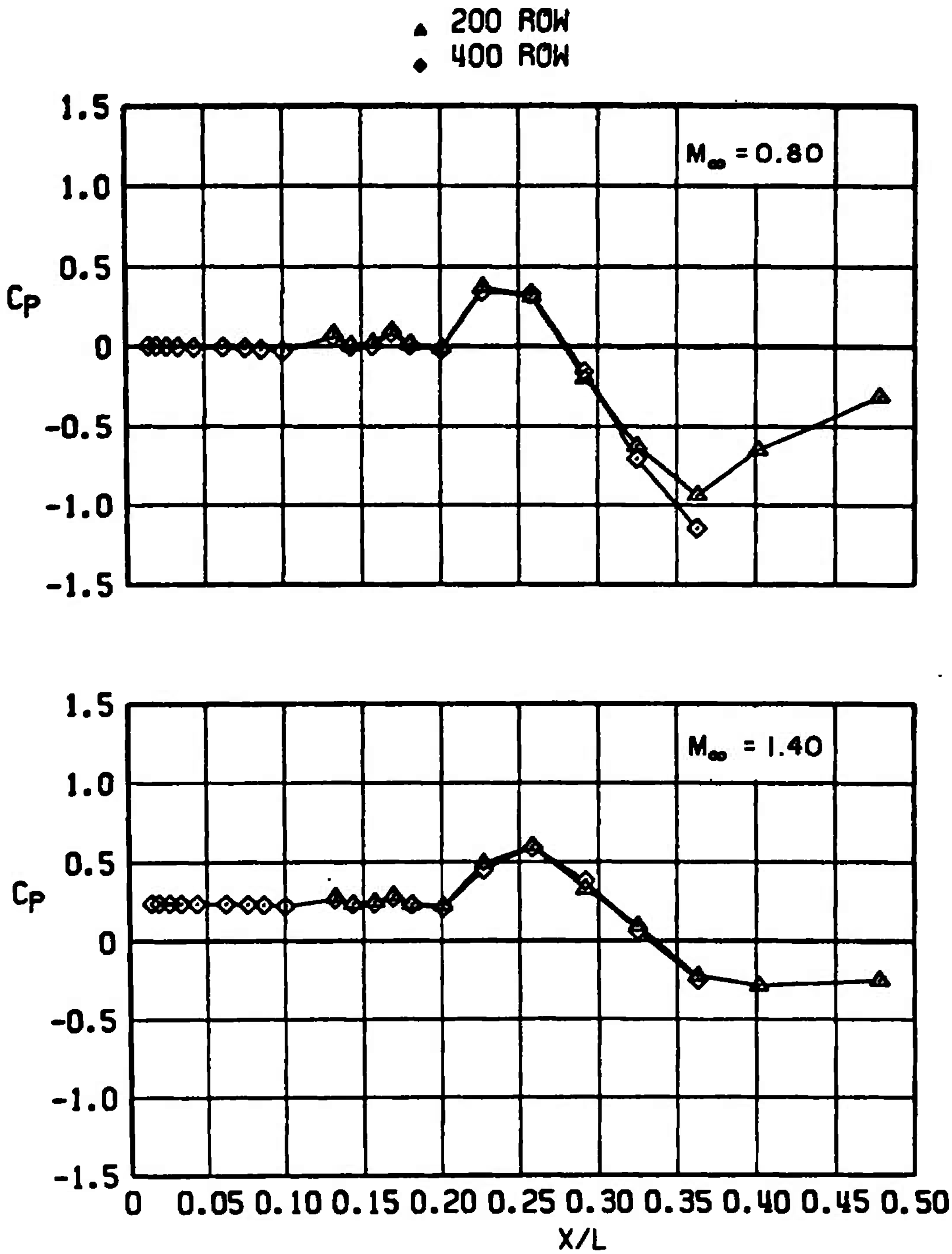

Figure 15. Concluded.

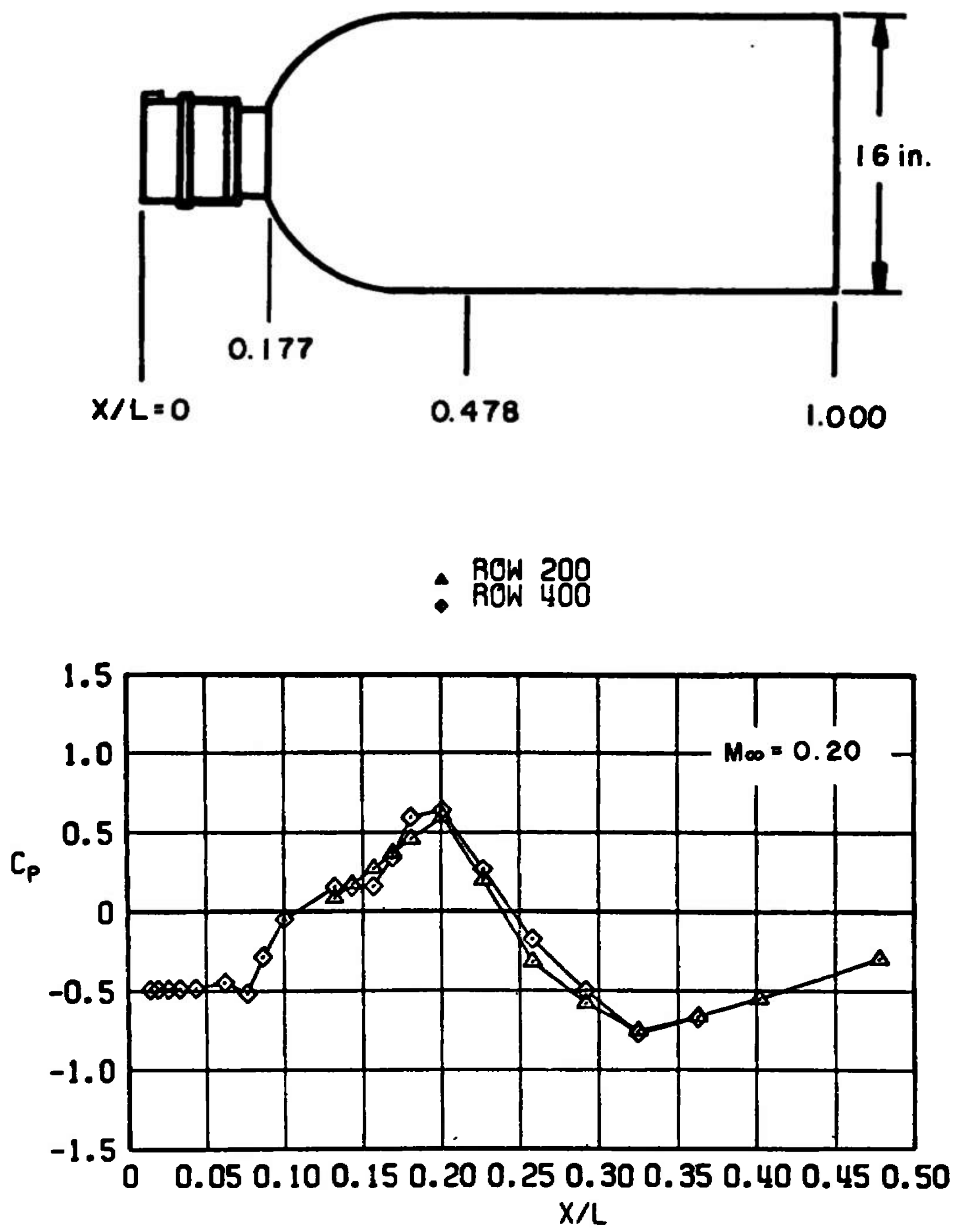

Figure 16. Variation of pressure coefficient along the two side rows of the radome-bomb body at 10-deg angle of attack.

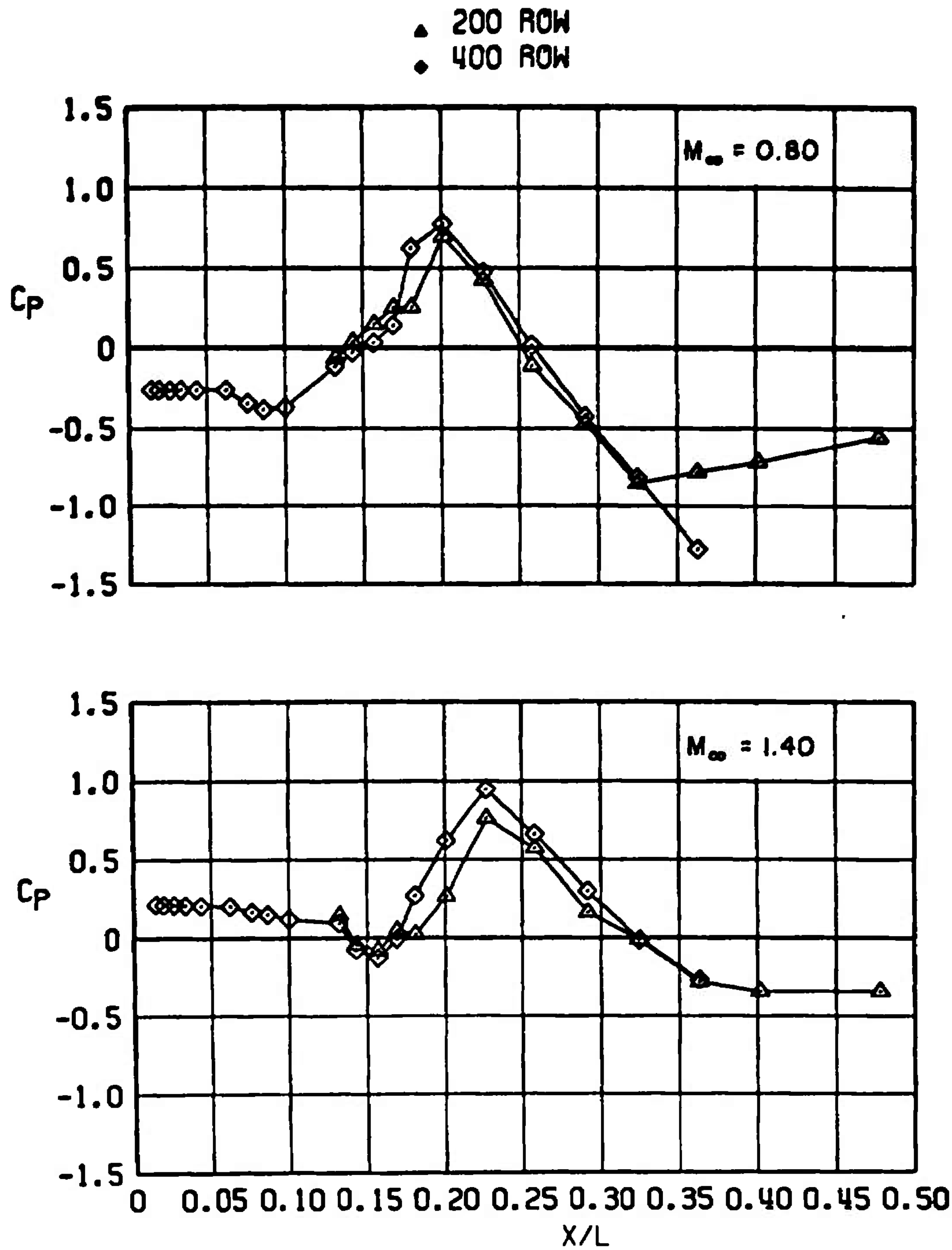

Figure 16. Concluded.

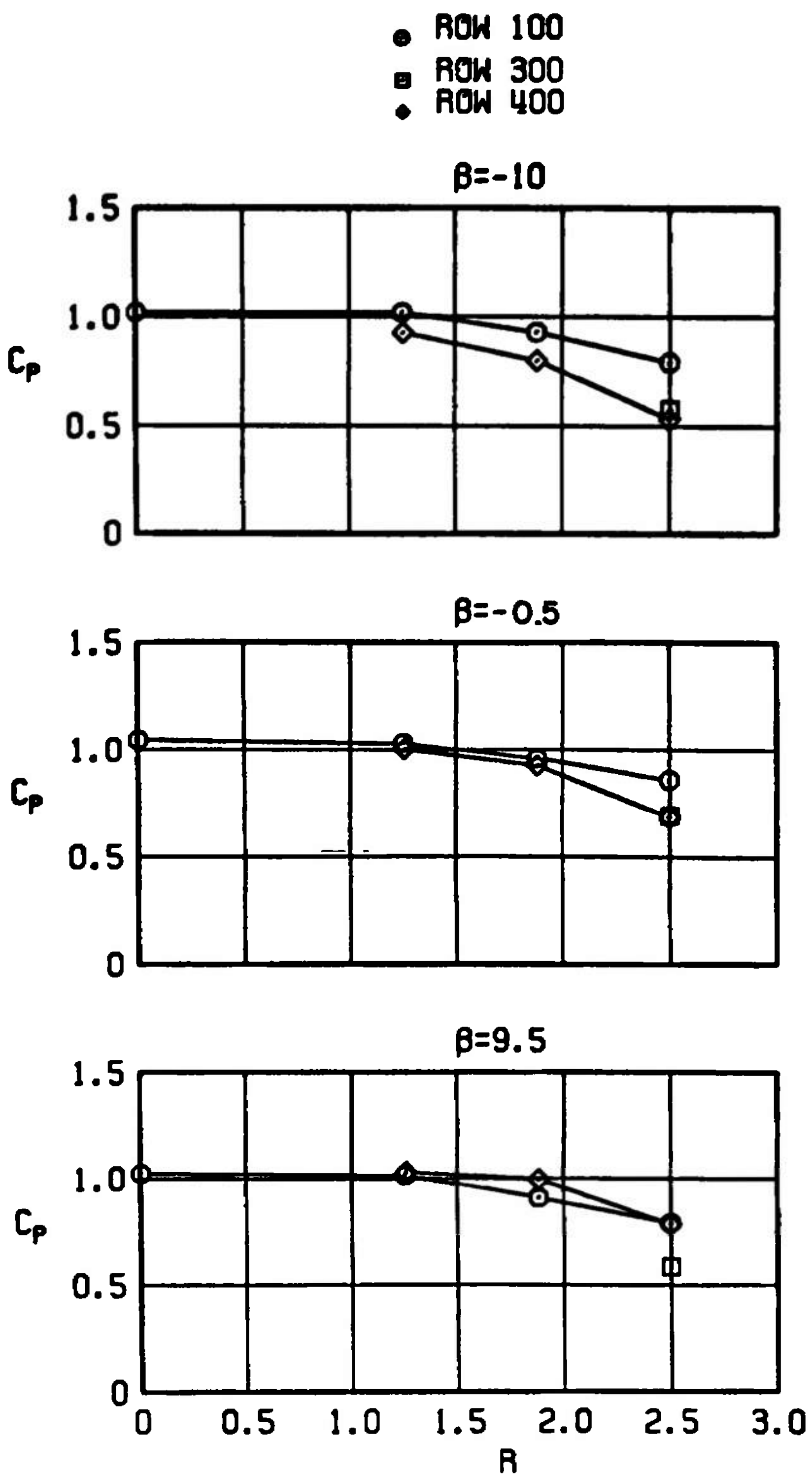

a. $M_\infty = 0.20$

Figure 17. Effect of angle of sideslip on the pressure profiles on the radome face.

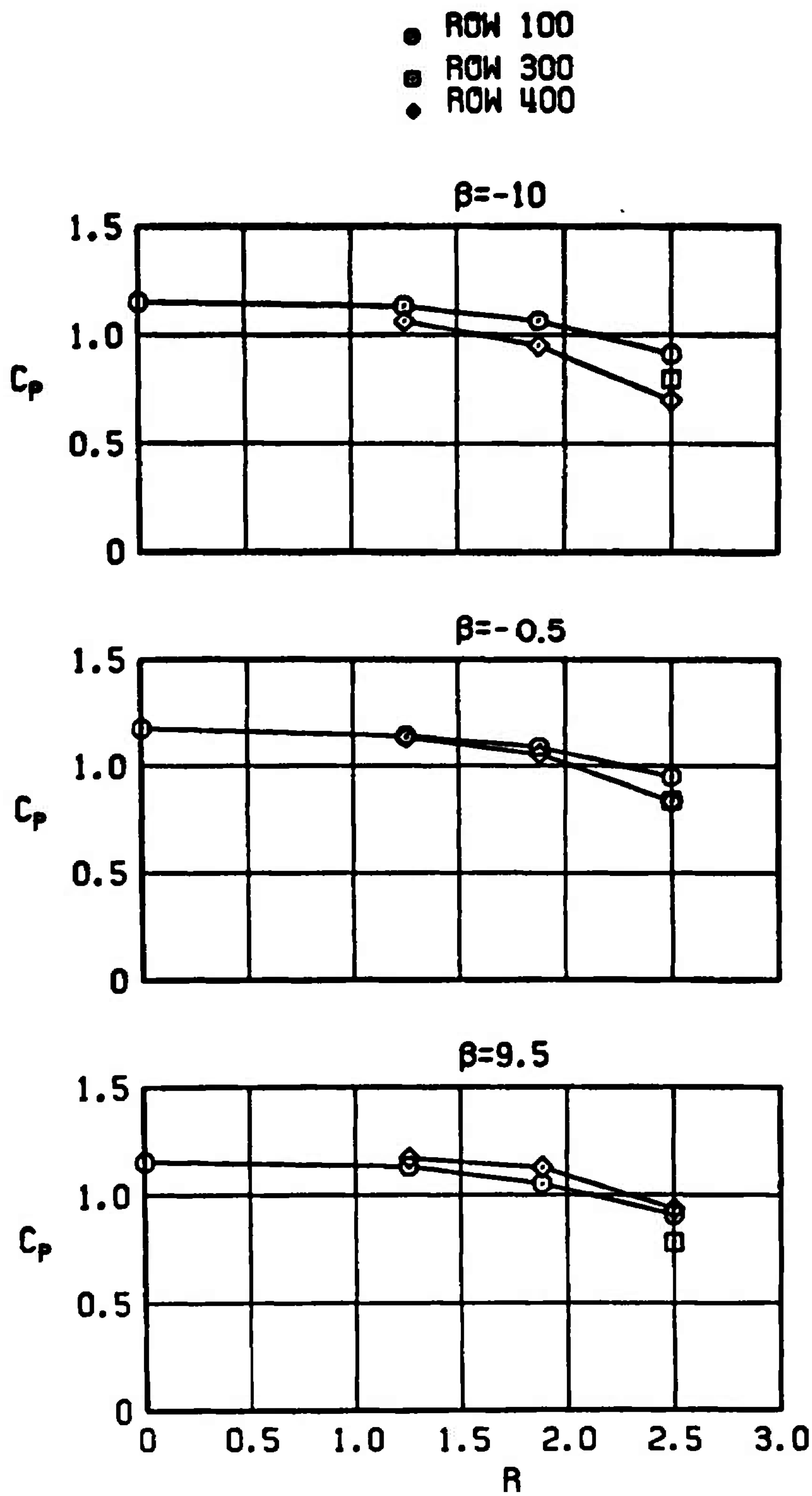

b. $M_\infty = 0.80$
Figure 17. Continued.

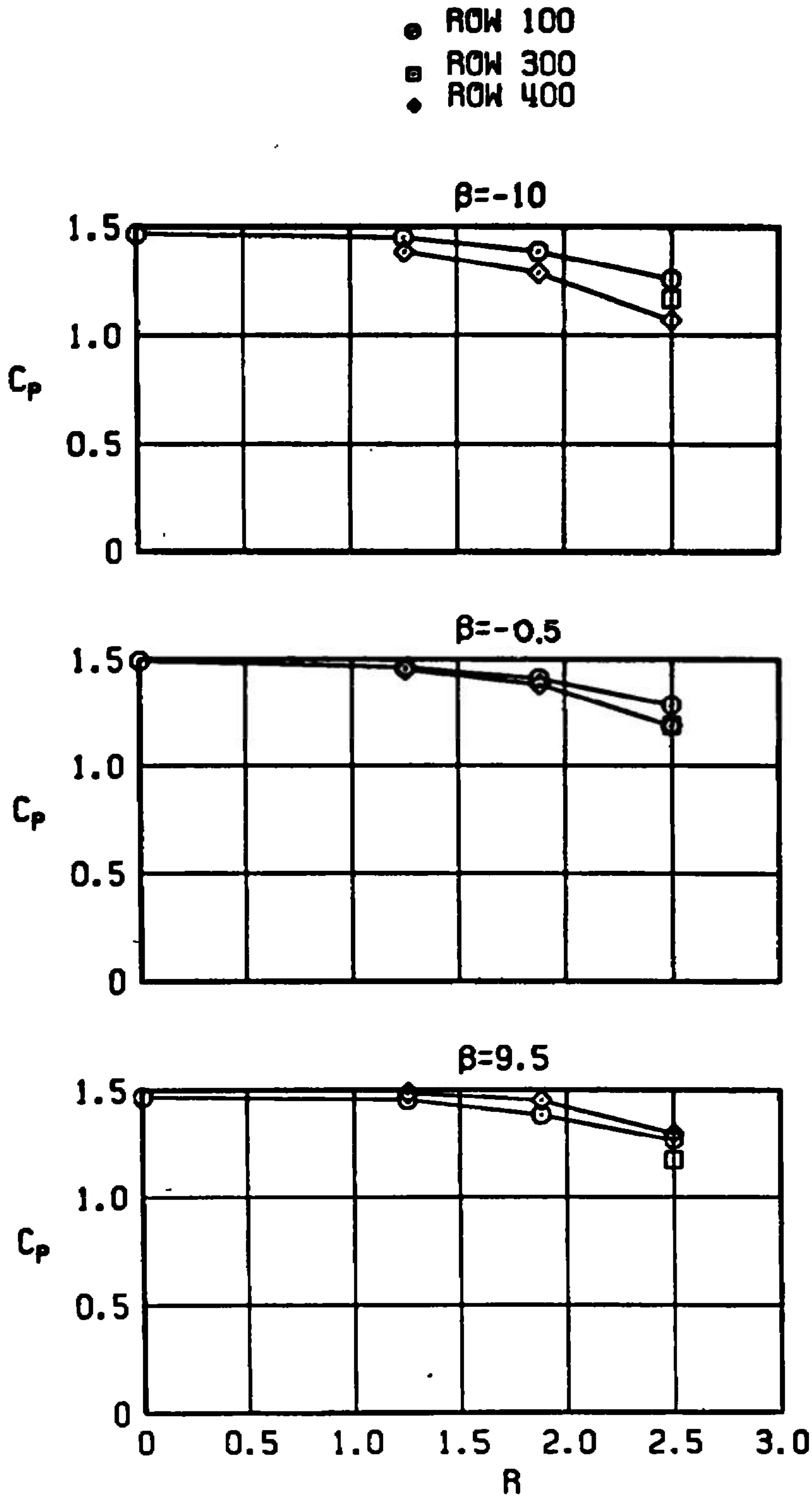

c. $M_\infty = 1.40$
Figure 17. Concluded.

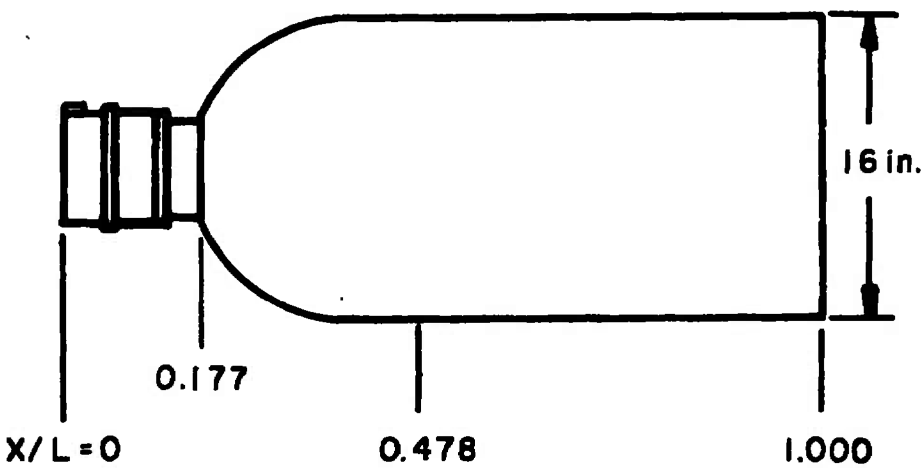

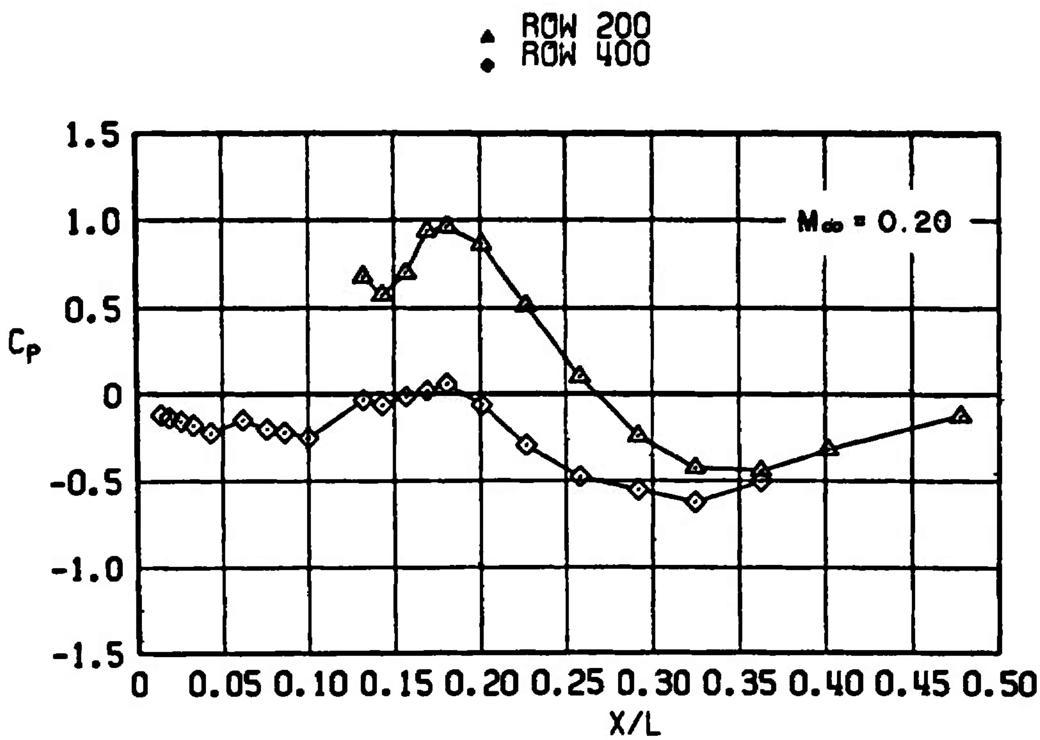

Figure 18. Pressure profiles along the top and bottom rows of the radome-bomb body at -10-deg beta angle.

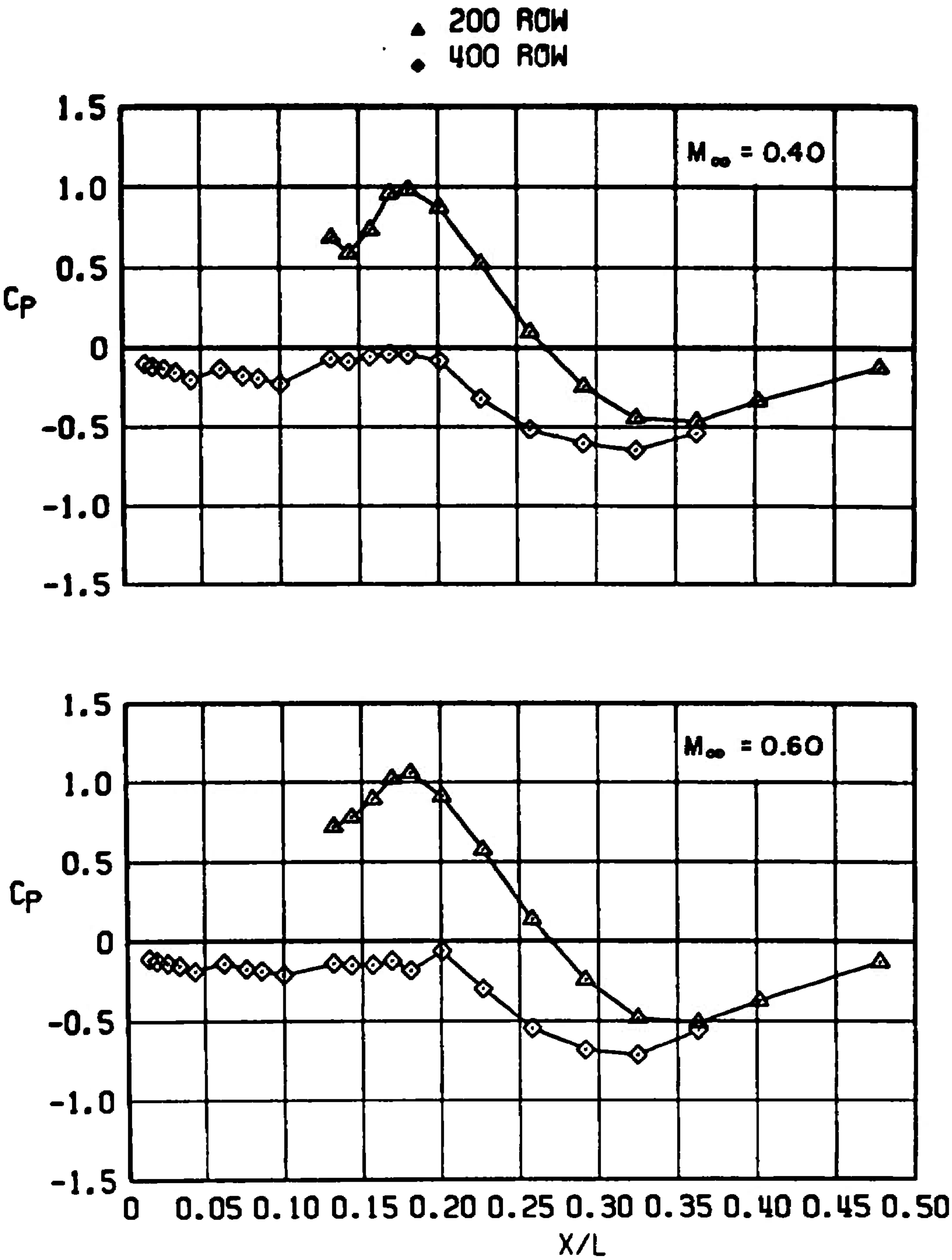

Figure 18. Continued.

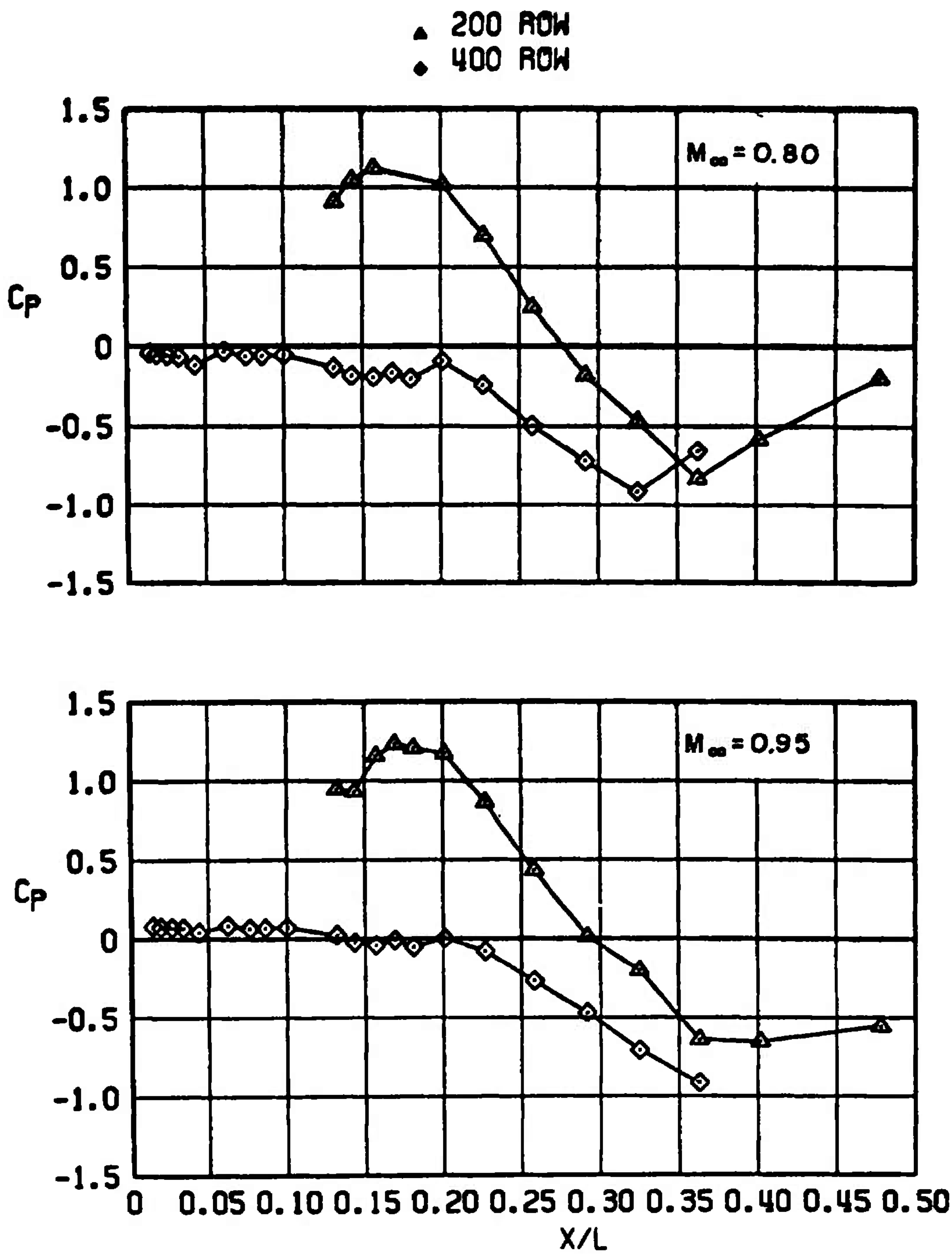

Figure 18. Continued.

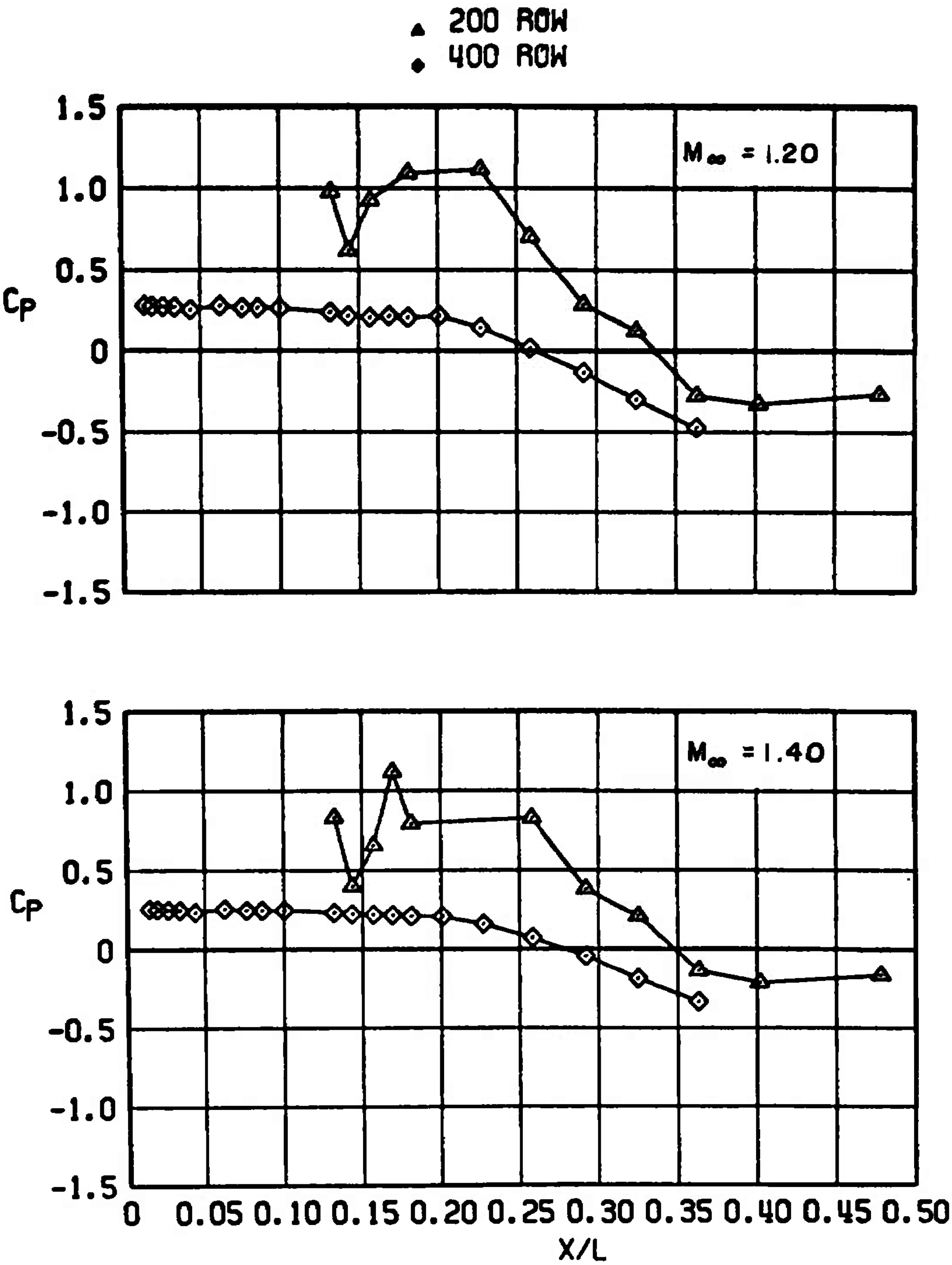

Figure 18. Concluded.

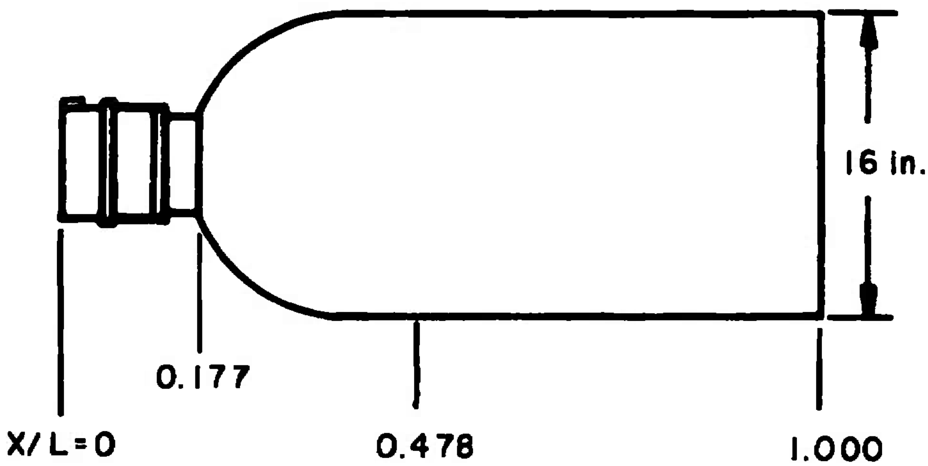

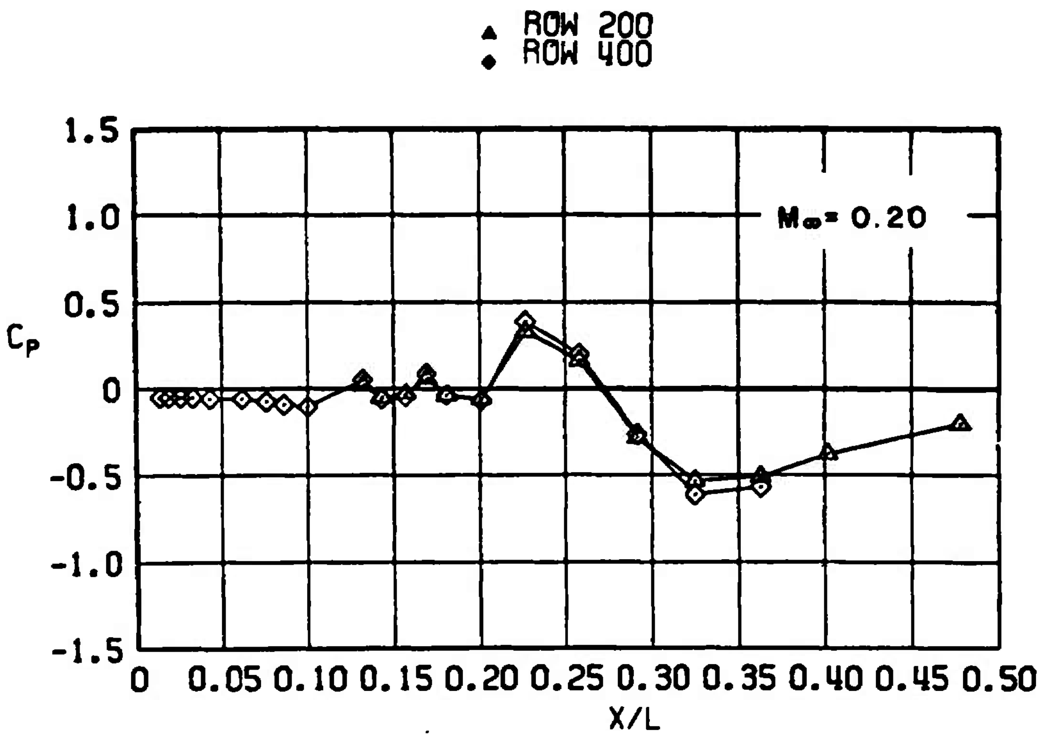

Figure 19. Pressure profiles along the top and bottom rows of the radome-bomb body at -0.5-deg beta angle.

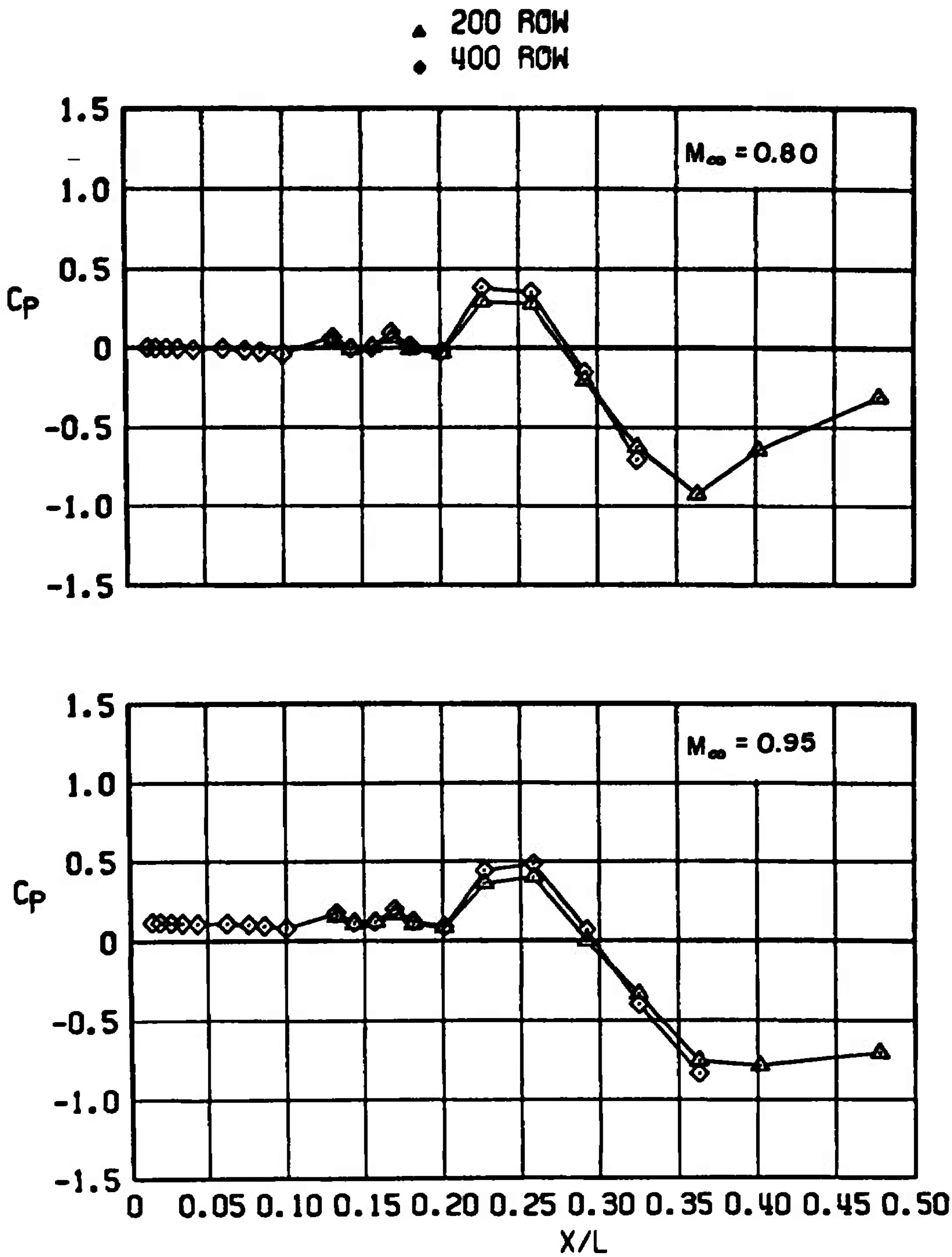

Figure 19. Continued.

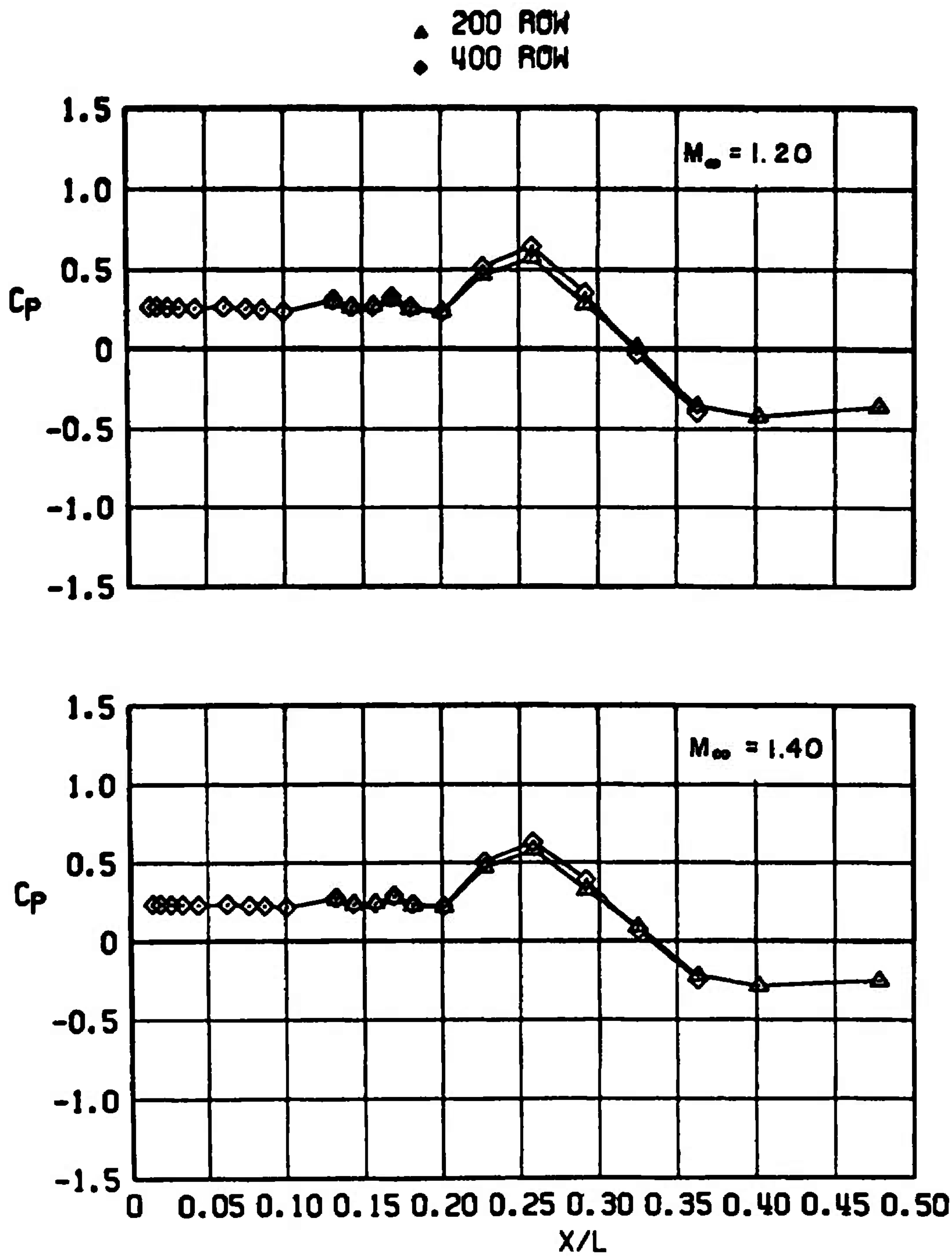

Figure 19. Concluded.

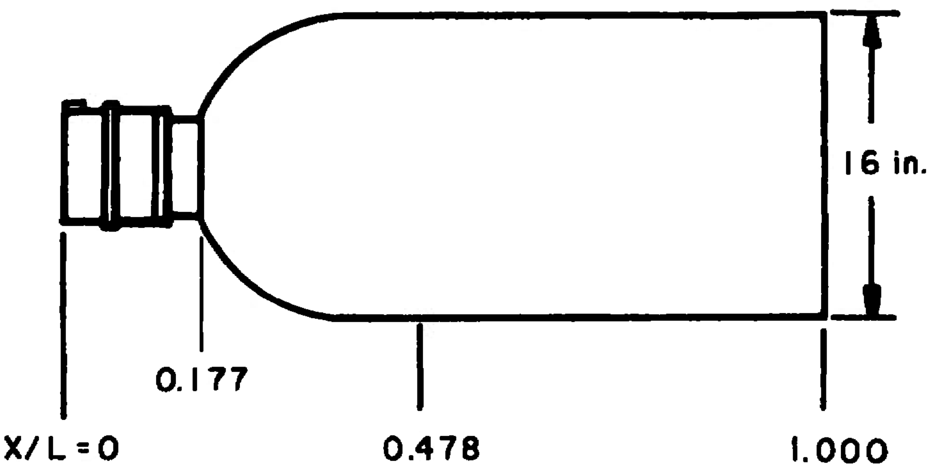

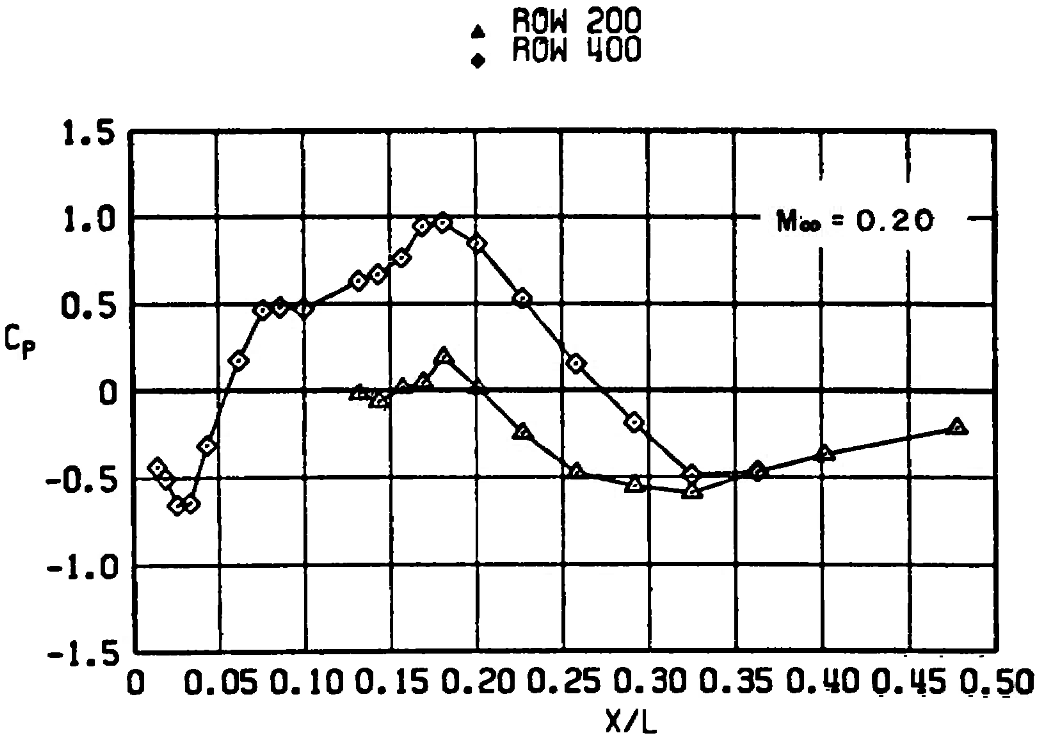

Figure 20. Pressure profiles along the top and bottom rows of the radome-bomb body at 9.5-deg beta angle.

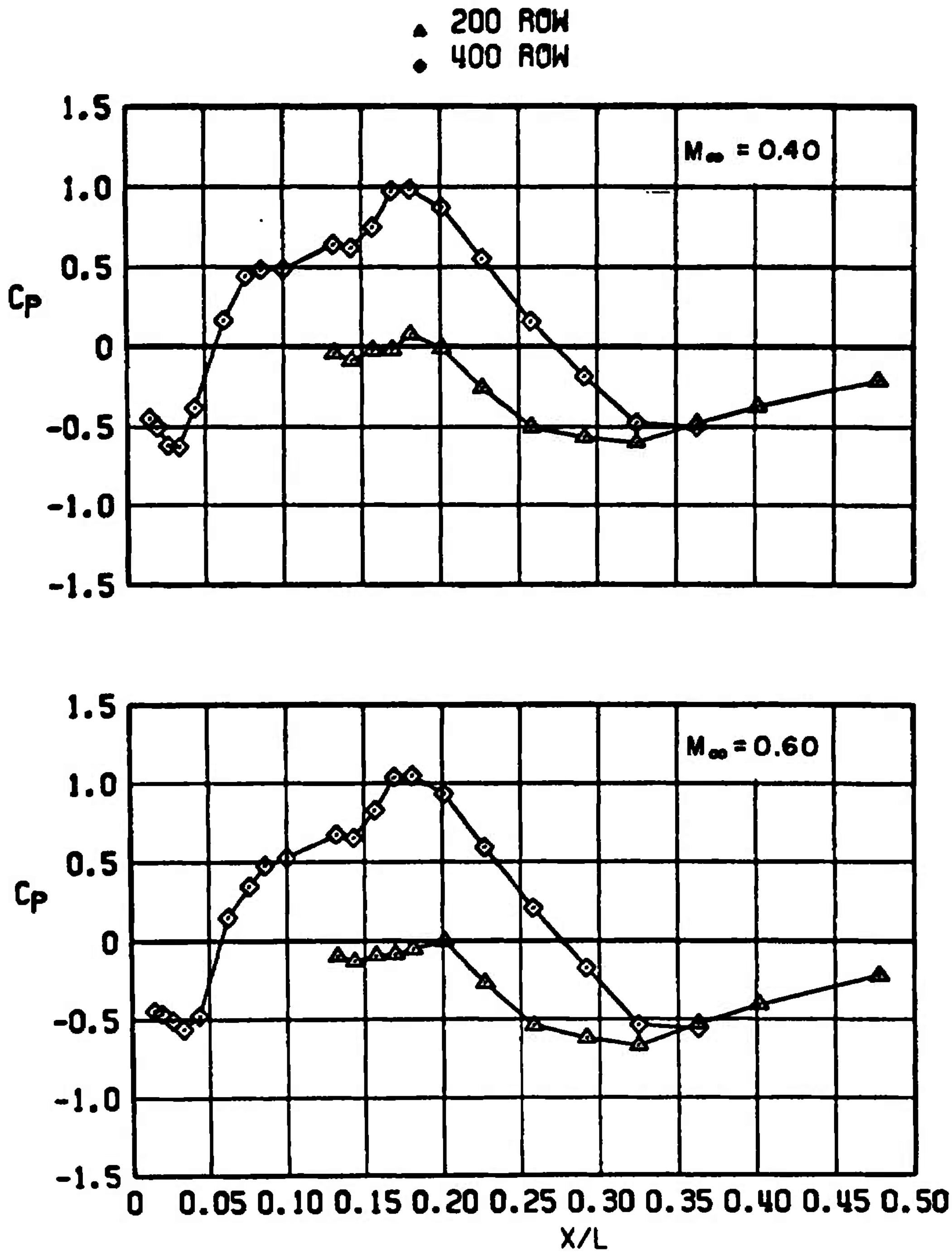

Figure 20. Continued.

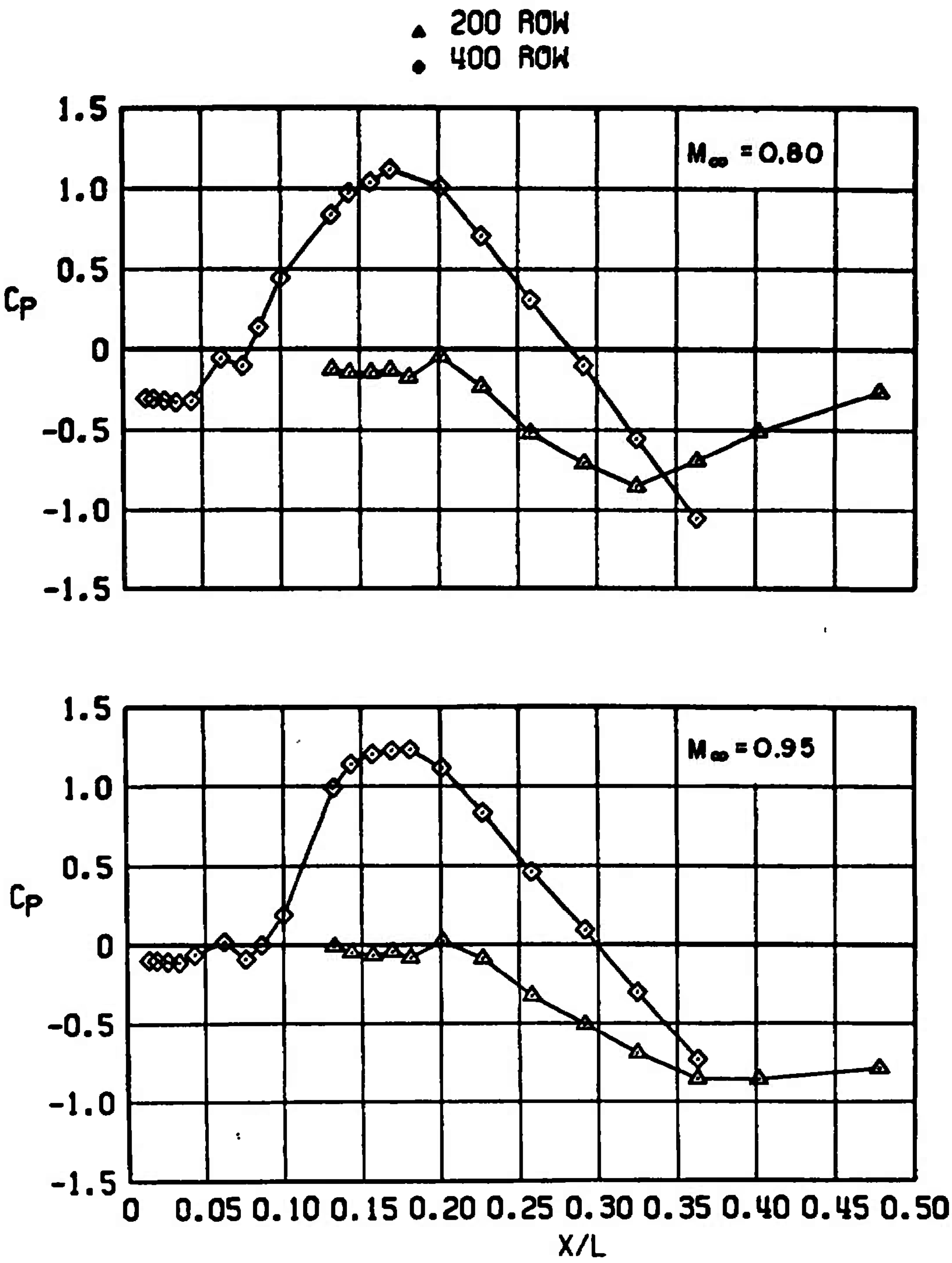

Figure 20. Continued.

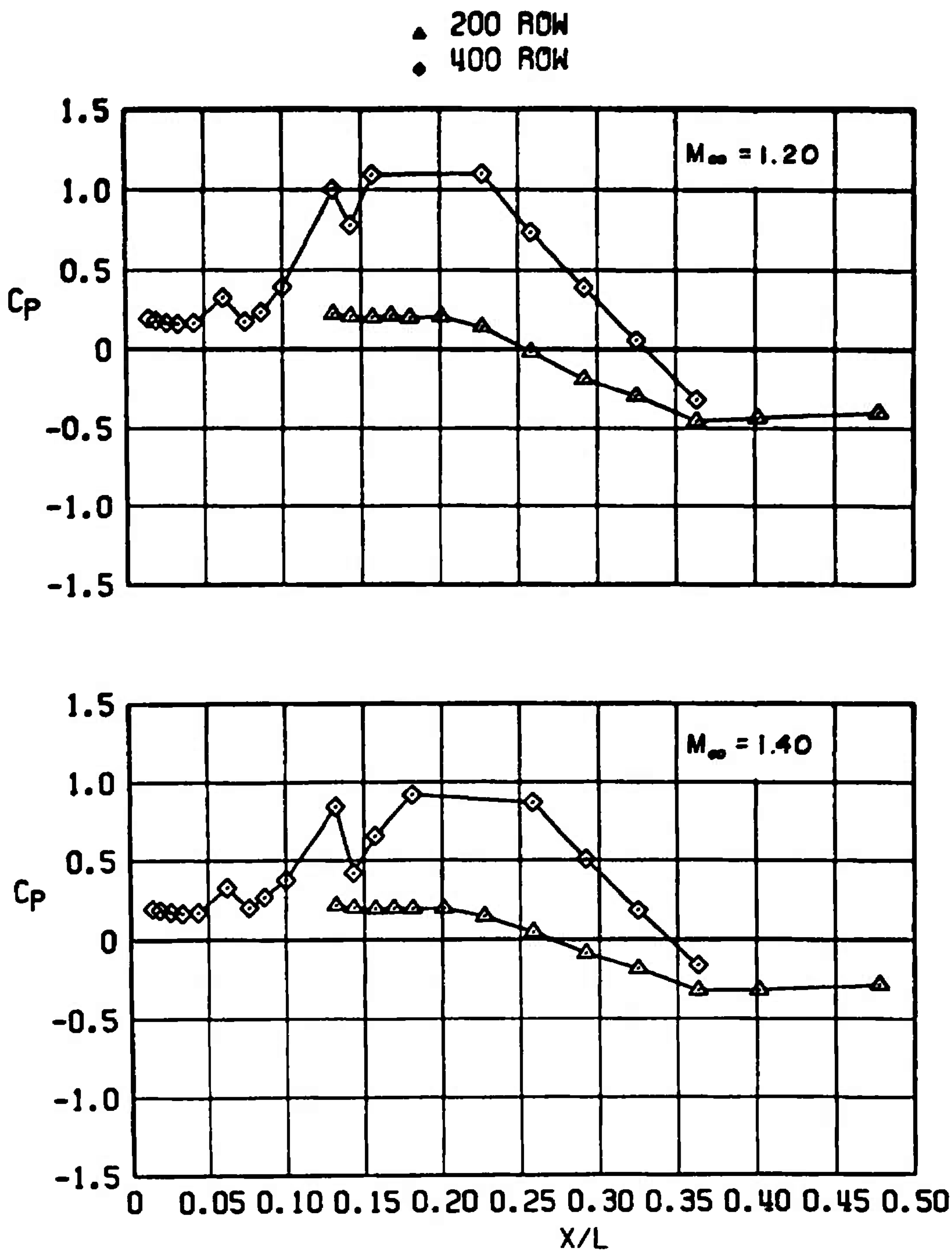

Figure 20. Concluded.

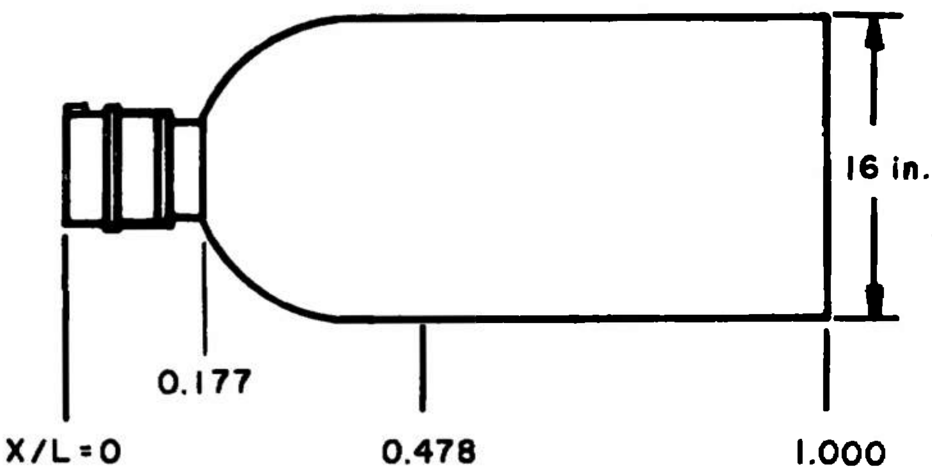

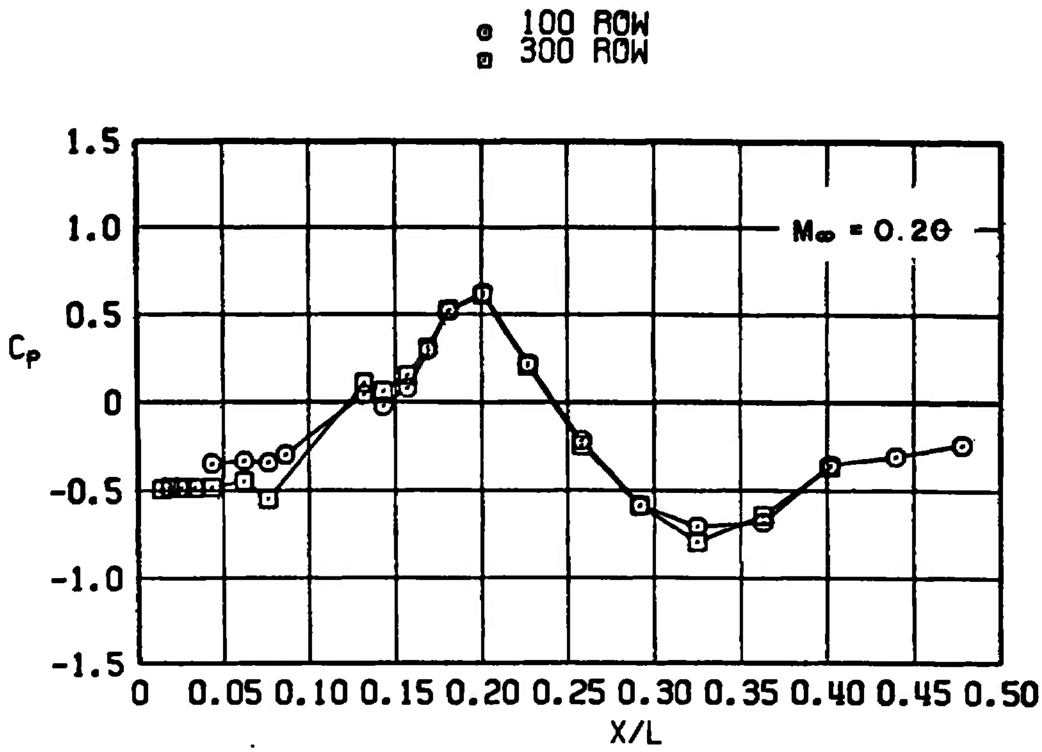

Figure 21. Variation of pressure coefficient along the two side rows of the radome-bomb body at -10-deg beta angle.

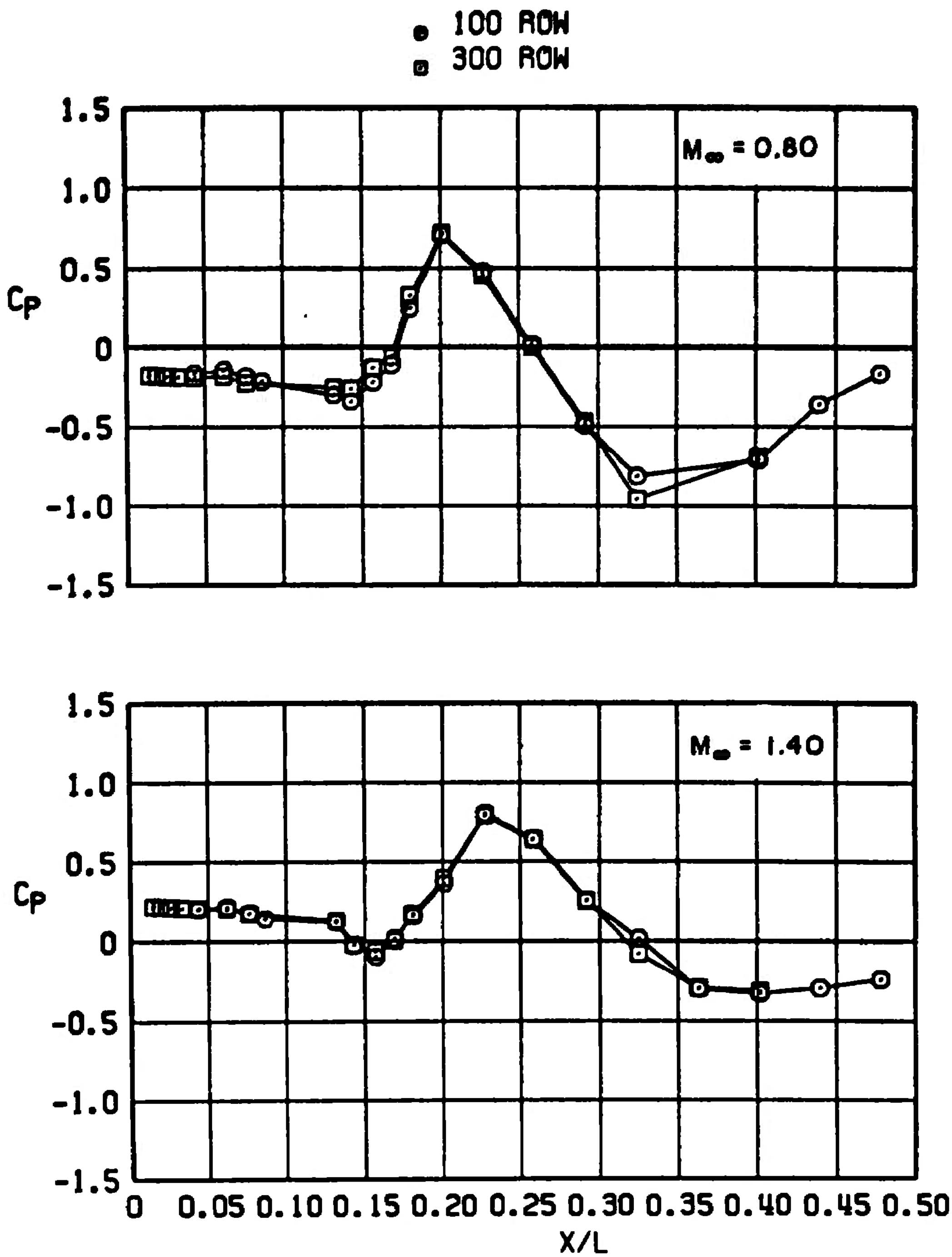

Figure 21. Concluded.

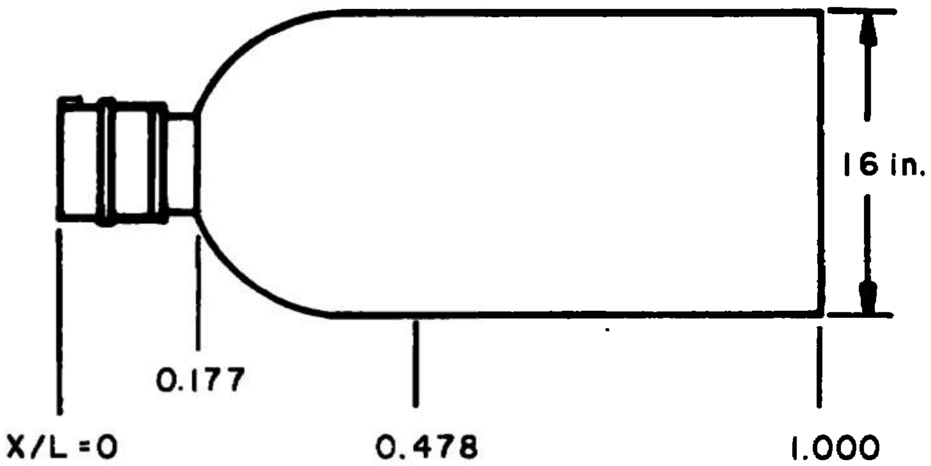

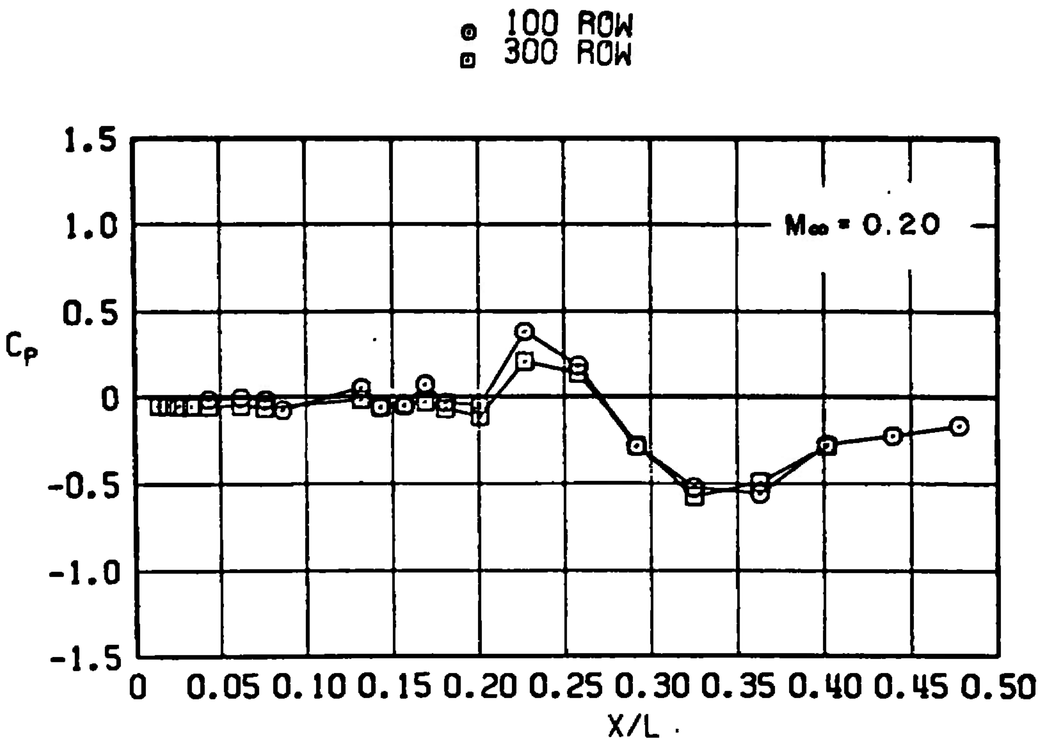

Figure 22. Variation of pressure coefficient along the two side rows of the radome-bomb body at -0.5-deg beta angle.

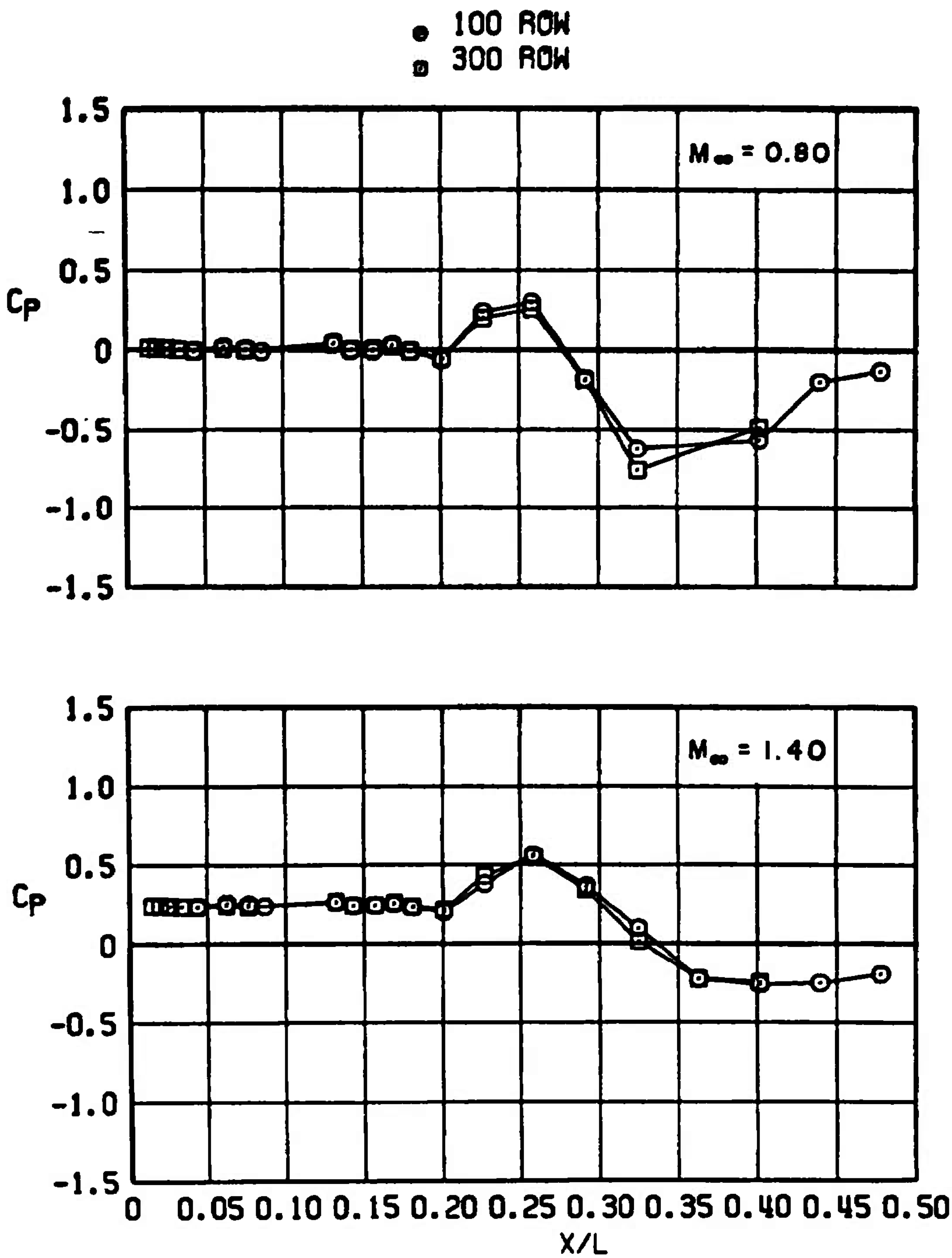

Figure 22. Concluded.

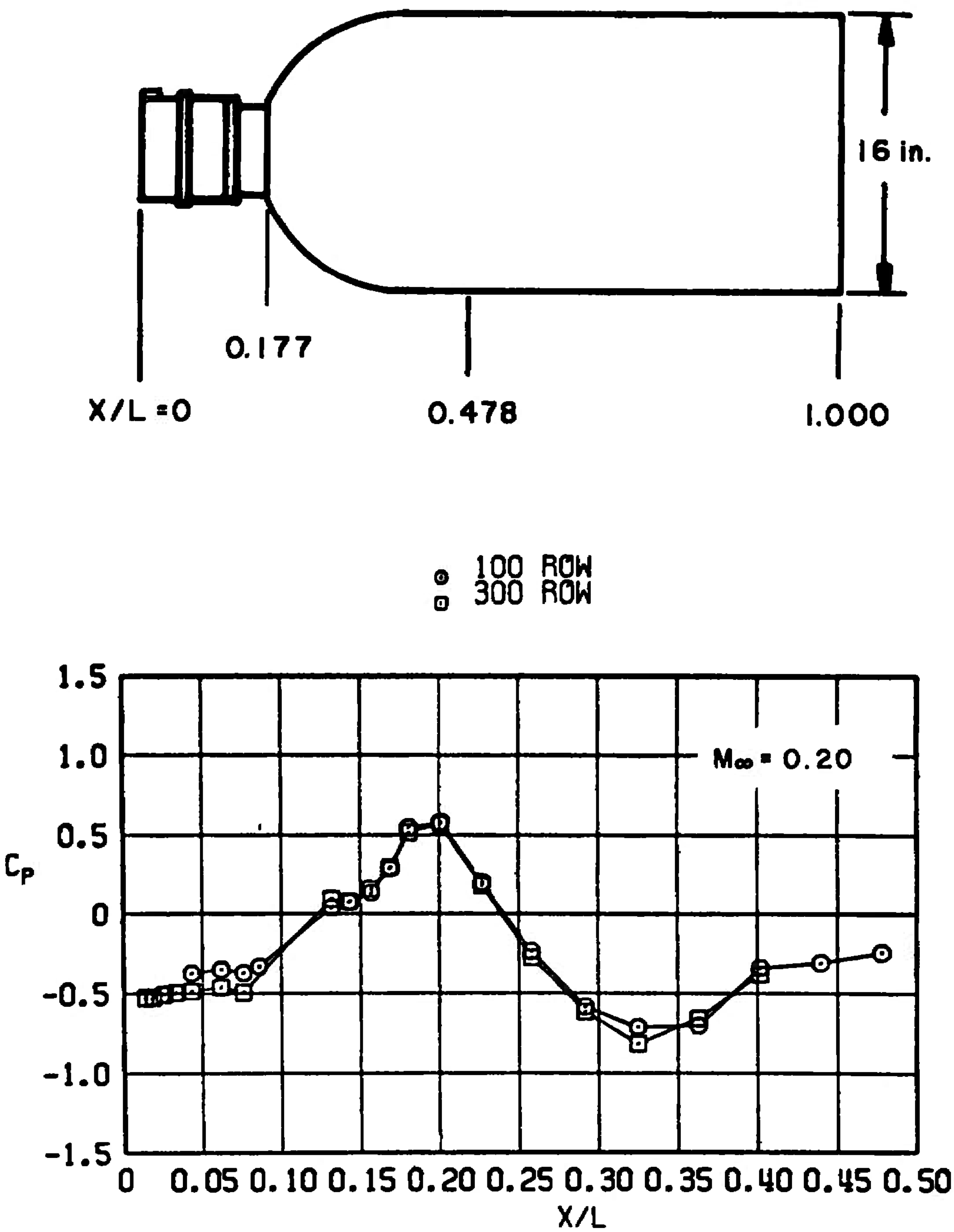

Figure 23. Variation of pressure coefficient along the two side rows of the radome-bomb body at 9.5-deg beta angle.

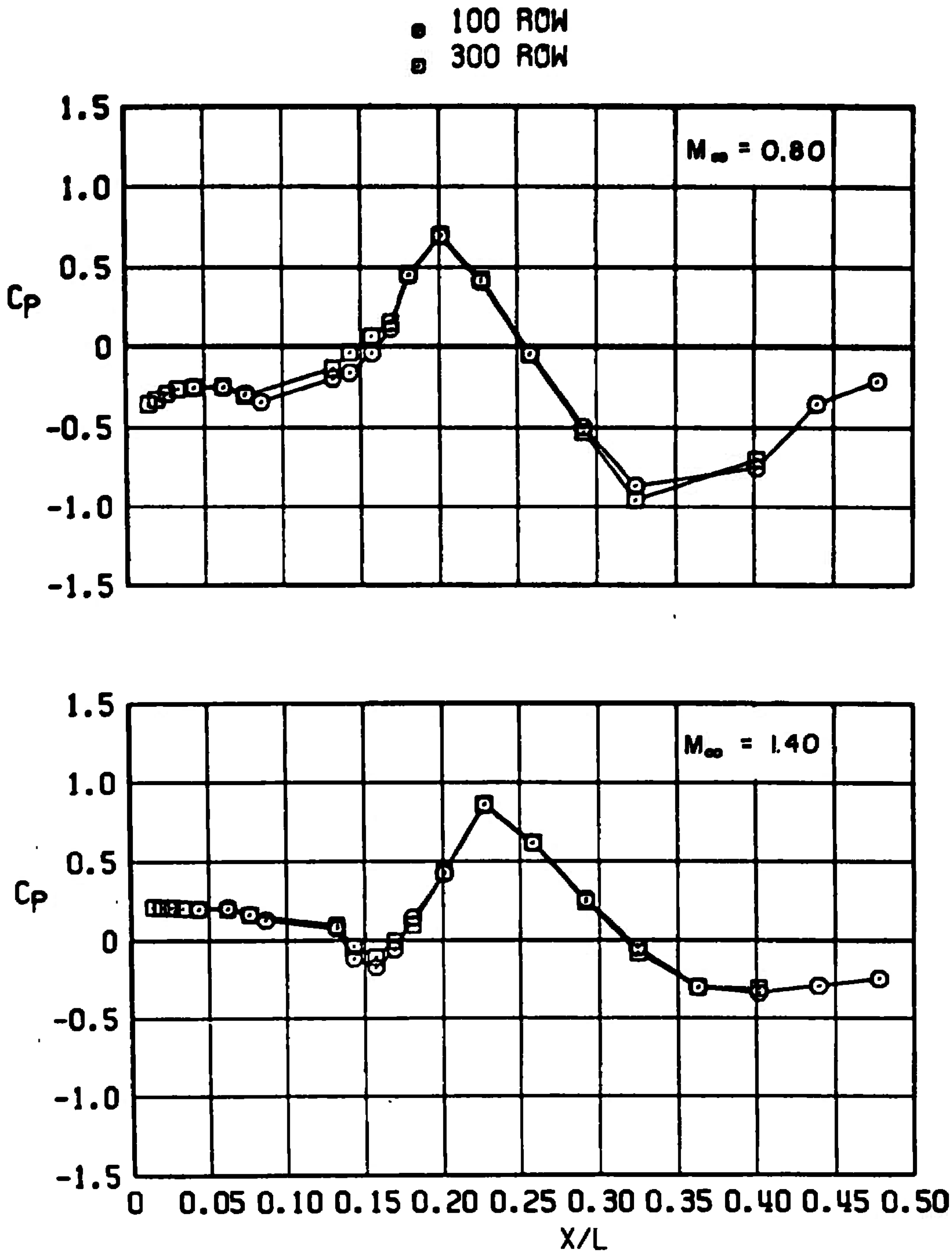

Figure 23. Concluded.

NOMENCLATURE

C_p	Pressure coefficient, $(P_i - P_\infty)/q_\infty$
DPH20	Venturi delta pressure PH20(3) - PH20(4), in. of water
M_∞	Free-stream Mach number
P_i	Local static pressure, psfa
P_∞	Free-stream static pressure, psfa
P_{t_∞}	Free-stream total pressure, psfa
q_∞	Free-stream dynamic pressure, psf
R	Radial distance of pressure orifice from model centerline, in..
$Re \times 10^{-6}$	Unit Reynolds number, per foot
x/L	Ratio of horizontal distance to pressure orifice divided by model length
$z \times 10^{-3}$	Pressure altitude, ft
α	Angle of attack (alpha), deg
β	Sideslip angle (beta), deg
θ	Radial angle for location of pressure rows (counterclockwise from zero), deg
ϕ	Model roll angle, deg